How many markers are needed to robustly determine a cell's type?

Stephan Fischer[1] and Jesse Gillis[1,2,*]

[1]Cold Spring Harbor Laboratory, Stanley Institute for Cognitive Genomics, Cold Spring Harbor, NY 11724, USA

[2]Cold Spring Harbor Laboratory, Watson School of Biological Sciences, Cold Spring Harbor, NY, USA

*Correspondence: jgillis@cshl.edu

Summary

Our understanding of cell types has advanced considerably with the publication of single cell atlases. Marker genes play an essential role for experimental validation and computational analyses such as physiological characterization through pathway enrichment, annotation, and deconvolution. However, a framework for quantifying marker replicability and picking replicable markers is currently lacking. Here, using high quality data from the Brain Initiative Cell Census Network (BICCN), we systematically investigate marker replicability for 85 neuronal cell types. We show that, due to dataset-specific noise, we need to combine 5 datasets to obtain robust differentially expressed (DE) genes, particularly for rare populations and lowly expressed genes. We estimate that 10 to 200 meta-analytic markers provide optimal performance in downstream computational tasks. Replicable marker lists condense single cell atlases into interpretable and generalizable information about cell types, opening avenues for downstream applications, including cell type annotation, selection of gene panels and bulk data deconvolution.

Keywords

Cell types, single-cell RNA sequencing, replicability, marker genes, cell type taxonomy.

Introduction

Recent atlas efforts based on single cell technologies have led to comprehensive cell type taxonomies that include a multitude of novel cell types (Tasic et al. 2018; Zeisel et al. 2018; Schaum et al. 2018; Packer et al. 2019; Cao et al. 2020). The discovery of new cell types and novel biological heterogeneity served as a foundation for promising avenues for the understanding of tissue homeostasis and disease. However, to develop downstream applications and experiments, an actionable description of cell types is required that extends beyond taxonomic classification. While sporadic post-hoc markers are published alongside taxonomies, the replicability of these markers is rarely assessed. Here, we systematically evaluate marker replicability and propose unprecedented lists of replicable markers (or meta-markers) for neuronal cell types by selecting an optimal number of robustly upregulated genes across a compendium of brain datasets.

Given the rapid progression in the number and size of single-cell datasets (Svensson et al. 2018), making atlases easily accessible is an increasingly difficult challenge. Cell type centroids provide an efficient summary of active gene expression programs (Zeisel et al. 2018), but they are subject to batch effects (Tung et al. 2017) and discard expression variability. While integrative methods have been successful at mitigating batch effects for the joint analysis of a small groups of datasets (Butler et al. 2018; Haghverdi et al. 2018; Welch et al. 2019; Korsunsky et al. 2019; Lin et al. 2019) and the transfer of cell type annotations (Kiselev et al. 2018; Stuart et al. 2019), the abstract embedding of cell types is costly, as well as difficult to interpret and to extract for downstream applications. In contrast, markers provide an interpretable common denominator that does not involve data re-analysis or complex mathematical transformations; they are commonly used for functional

44 characterization (Mancarci et al. 2017), cell type annotation (Poulin et al. 2016; Johnson and Walsh
45 2017; Pliner et al. 2019; Zhang et al. 2019), deconvolution of bulk data (Wang et al. 2019; Newman
46 et al. 2019; Patrick et al. 2020) and spatial data (Qian et al. 2020), selection of representative gene
47 panels (Moffitt et al. 2018), cross-species comparisons (Tosches et al. 2018; Hodge et al. 2019;
48 Krienen et al. 2019; Bakken et al. 2020), and mapping of organoids to in vivo progenitors (Velasco et
49 al. 2019; Bhaduri et al. 2020). For many of these applications, the strength of individual markers is
50 limited by the lack of conservation (Bakken et al. 2020) and the sporadic expression in individual
51 cells (Kharchenko et al. 2014; Risso et al. 2018; Hicks et al. 2018; Chen and Zhou 2018). Moving past
52 individual markers to small lists is done sporadically to capture combinatorial relationships or
53 improve power, but has not yet exploited the full power of scRNA-seq data. In specific, because cell
54 types are encoded in a low-dimensional expression space (Crow and Gillis 2018), we hypothesize
55 that they can be captured with high resolution and generalizable definitions using redundant and
56 robust marker lists. These lists can then easily be compared and combined across datasets for
57 downstream analyses.

58 The problem of finding generalizable descriptions of cell types has a long history in the brain,
59 famously illustrated by Ramon y Cajal's morphology-based descriptions (RAMON Y CAJAL 1904).
60 More recently, the Petilla convention emphasized the need to describe neurons according to a multi-
61 modal taxonomy, including morphology, electrophysiology, connectivity and transcriptomics (Ascoli
62 et al. 2008). Single cell data, while only covering one aspect of this multi-modal description, have
63 enabled unprecedented wide and deep sampling of brain cells, with current taxonomies containing
64 several hundred cell types (Tasic et al. 2018; Zeisel et al. 2018). They thus offer a chance to assess
65 the robustness of transcriptomic cell types, but current cell types are usually defined based on data
66 from a single lab and a single computational method, while an ideal description should be
67 community-based and method-independent (Yuste et al. 2020). With the recent publication of
68 several single-cell compendia by the Brain Initiative Cell Census Network (BICCN)(Yao et al. 2020a,
69 2020b), the brain offers a unique opportunity to characterize marker-based descriptions.

70 In this manuscript, we systematically assess the replicability of markers for BICCN cell types. We
71 identify robust markers (meta-markers) across a compendium of 7 brain single cell datasets
72 containing a total of 482,712 cells from the BICCN, one of the most complex and comprehensive cell
73 type taxonomies to date. The assessment procedure is based on two simple steps: (i) identify
74 markers from single datasets, (ii) obtain a list of meta-markers by selecting replicable markers. The
75 compendium samples from 6 single-cell and single-nuclei technologies, resulting in meta-markers
76 that are robust to the varying sensitivity and contamination levels of these technologies. We further
77 investigate the ability of markers to recapitulate cell types at various levels of granularity. We define
78 two simple performance axes, intuitively representing coverage (being expressed in all cells of
79 interest) and signal-to-noise ratio (being expressed exclusively in cells of interest), that can be
80 efficiently summarized using standard differential expression statistics. While individual meta-
81 markers only imperfectly capture cell types, we find that aggregating 10 to 200 meta-markers leads
82 to optimal performance in downstream computational analyses, such as cell type annotation and
83 deconvolution. Remarkably, these marker-based descriptions, derived from the primary motor
84 cortex, generalize to other cortical brain regions, enabling accurate annotation of individual cells.
85 Robust meta-markers thus provide a simple and actionable description of BICCN cell types, which we
86 make available as high-quality marker lists (Sup. Data 1-3) ranging from the lowest resolution
87 (excitatory neurons, inhibitory neurons, non-neurons) to the finest resolution defined by the BICCN
88 (85 neuronal cell types).

89 Results

90 The ideal marker gene fulfills two criteria: (1) it is expressed in all cells of the population of interest,
91 providing high coverage, (2) it is not expressed in background cells, providing a high signal-to-noise
92 ratio (Fig. 1a). In recently published atlases, it is often unclear how strongly and robustly the
93 proposed markers fulfill these criteria, particularly at high clustering resolution. To investigate
94 replicability of marker strength, our basic strategy is to look for simple statistics that can be robustly

95 averaged across datasets and correctly capture coverage and signal-to-noise. We focused on a BICCN
96 neuron atlas containing 7 datasets with 482,712 cells, organized into a hierarchy of 116 cell types in
97 3 levels of increasing resolution: classes, subclasses and clusters (Yao et al. 2020a)(Table 1).

Dataset	Brain regions	Assay	Technology	# cells	# cell types	# genes detected	# UMIs / reads
scSS	MOp	Cell	SmartSeq	6,288	61	9,420	1,750,664
snSS	MOp	Nucleus	SmartSeq	6,171	46	4,363	613,762
scCv2	MOp	Cell	10X v2	122,641	90	4,594	12,697
snCv2	MOp	Nucleus	10X v2	76,525	43	1,716	3,145
snCv3M	MOp	Nucleus	10X v3	159,738	113	4,237	12,060
scCv3	MOp	Cell	10X v3	71,183	78	7,282	46,148
snCv3Z	MOp	Nucleus	10X v3	40,166	67	3,445	16,088
AUD	AUD	Cell	10X v2	71,670	203	3,969	10,105
Isocortex-Hippocampus	21	Cell	SmartSeq	827 to 16,318	13 to 183	6,099 to 9,006	488,099 to 2,016,775
Isocortex-Hippocampus	19	Cell	10X v2	18,307 to 216,203	166 to 263	2,874 to 4,944	6,102 to 15,272

98 ***Table 1. List of Brain Initiative Cell Census Network (BICCN) datasets used in this study.*** *All datasets are from*
99 *mouse. MOp corresponds to the primary motor cortex, AUD to the auditory cortex. The "# genes detected"*
100 *column contains the median number of genes detected per cell. The "# UMI / reads" column contains either the*
101 *median number of reads per cell (for SmartSeq datasets) or the median number of UMIs per cell (for 10X*
102 *datasets).*

103 Meta-analytic markers are highly replicable

104 We started by investigating the replicability of standard differential expression (DE) statistics across
105 BICCN datasets. Previous experiments in microarray and bulk RNAseq data by the MAQC (Shi et al.
106 2006) and SEQC (Consortium et al. 2014) consortia established that a fold change (FC) threshold
107 between 2 and 4 was necessary to obtain replicable DE genes. We wondered if a similar threshold
108 would hold for single cell RNAseq and how aggregation across datasets would improve the threshold
109 for fold change (FC) and the area under the receiver-operator curve (AUROC), a statistic routinely
110 used to compute the statistical significance of DE.

111 To assess the replicability of FC, we quantified how often one would draw inconsistent conclusions
112 about a significant DE gene being upregulated (type S error (Gelman and Carlin 2014)). For example,
113 given that I observed a gene with FC=2 (strongly upregulated), what is the probability that my gene
114 will have a FC<1 (downregulated) in an independent experiment? When FC was estimated from a

single dataset, as is routine in published studies, we found that a threshold of FC>4 was necessary to call a gene reliably upregulated (type S error < 5%, Fig. 1b), in line with MAQC/SEQC conclusions. In contrast, estimating FC from a higher number of datasets dramatically improved replicability: for 2 datasets the 5% error threshold is reached at FC > 2, for 3 datasets at FC > 1.5. Surprisingly, for more than 5 datasets, our results suggest that thresholding becomes unnecessary: a gene that was detected as upregulated in 5 independent datasets was almost always upregulated in the 2 remaining datasets, even at low effect size (FC~1). Moreover, for a single dataset, only the top 10 upregulated genes were replicable, while the top 1000 genes are reliably upregulated when aggregating across 6 datasets (Sup. Fig. 1b). We observed similar trends for AUROCs. Based on a single dataset, the replicability threshold was AUROC>0.65, yielding 100 reliably upregulated genes. Aggregating six datasets, no replicability threshold was needed and we could identify more than 5000 reliably upregulated genes (Sup. Fig. 1a,c). The impact of dataset aggregation was particularly dramatic for small clusters and lowly expressed genes (Sup. Fig. 1d-g); for 5/85 neuron clusters, fewer than 5 of the top 10 single dataset markers (based on fold change) were reliably upregulated.

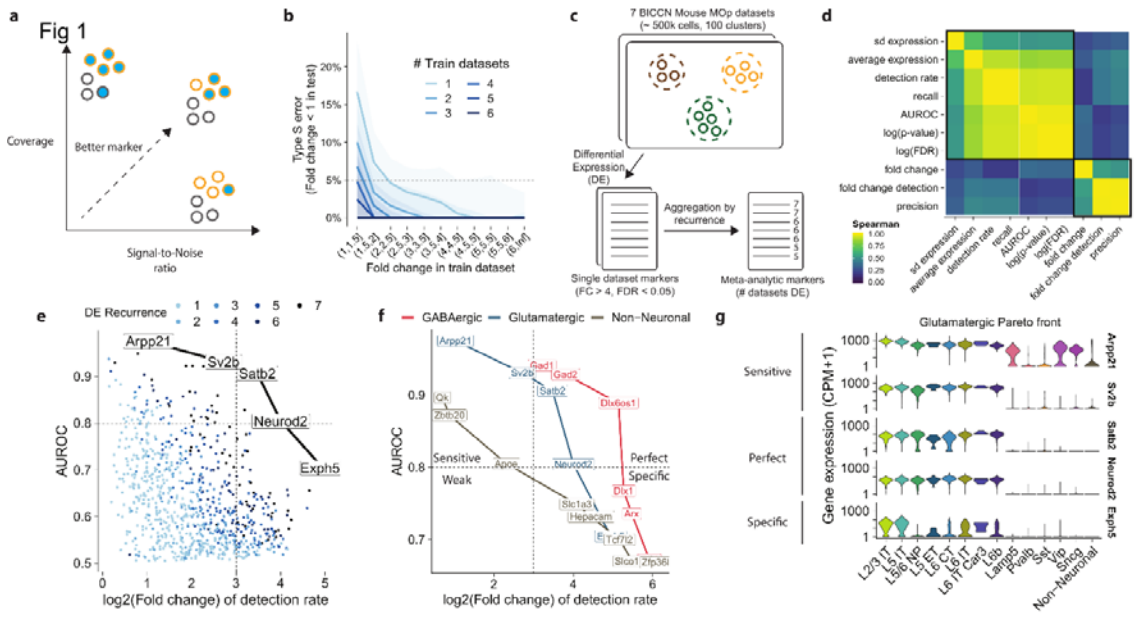

Figure 1. The meta-analytic Pareto front of markers: a trade-off between coverage and signal-to-noise ratio. a *Ideal markers have high coverage (high expression in cells of interest) and high signal-to-noise ratio (relatively low expression in background cells).* ***b*** *Fraction of genes inconsistently detected as upregulated (type S error) depending on the fold change in the training dataset. Colors indicate the number of datasets used to estimate the fold change (geometric mean).* ***c***

Schematic of extraction of meta-analytic markers: differentially expressed (DE) genes are computed independently in each dataset, meta-markers are selected based on the number of times they were DE across datasets. ***d*** *Spearman correlation of standard DE statistics for putative markers (averaged over datasets). We highlight two independent groups of statistics that can serve as a proxy for coverage and signal-to-noise ratio.* ***e*** *Recurrent DE genes in glutamatergic neurons, using AUROC as a proxy for coverage and fold change of detection rate as a proxy for signal-to-noise ratio. Gene names and lines highlight the Pareto front of markers, which offer optimal trade-off between signal-to-noise and coverage.* ***f*** *Pareto fronts for neuronal classes (glutamatergic neurons, GABAergic neurons and non-neuronal cells) in the coverage/signal-to-noise space. We subdivide markers as perfect (high coverage and signal-to-noise), specific, sensitive, or weak (low coverage and signal-to-noise).* ***g*** *Illustration of sensitive (high target expression, some background expression), perfect (high target expression, no background expression) and specific (low target expression, no background expression) markers along the glutamatergic Pareto front.*

No individual marker offers high coverage and signal-to-noise ratio

Having established that DE statistics are replicable in aggregate, we assessed a range of existing statistics and found they strongly clustered into two groups, corresponding to definitions for coverage and signal-to-noise ratio (Fig. 1c,d). The first block of statistics contained average gene expression and intuitively mapped to the notion of coverage; it also included the DE p-value and the detection rate, which are strongly indicative of genes that are broadly expressed. The second block contained the fold change and the fold change of detection rate and intuitively mapped to the notion of signal-to-noise ratio. The lack of correlation between the two blocks indicates that there is trade-off, genes have a “choice” between favoring coverage or signal-to-noise ratio. Note that this is broadly consistent with long-standing heuristic practice of considering both p-value and fold change in bulk DE through volcano plots (Cui and Churchill 2003; Goedhart and Luijsterburg 2020). In the following, we use the area under the receiver-operator characteristic curve (AUROC) as our proxy for coverage (as used in Seurat’s ROC test (Stuart et al. 2019) or LIGER’s marker detection (Welch et al. 2019; Liu et al. 2020)), fold change of the detection rate (FCd) as our proxy for signal-to-noise when we consider individual markers (as used in M3Drop (Andrews and Hemberg 2019)), and fold change (FC) as our proxy for signal-to-noise when we consider marker lists (as used in the traditional Volcano plot (Cui and Churchill 2003)).

In a FC/AUROC representation, genes offering a trade-off from best signal-to-noise marker to highest coverage marker form a Pareto front of markers (Fig. 1e). The Pareto front representation offers a rapid visualization of the strength of markers that can be associated with any given cell type. Based

165 on our exploration of the datasets, we subdivided markers as perfect (high coverage, AUROC > 0.8,
166 high signal-to-noise, FCd > 8), specific (high signal-to-noise), sensitive (high coverage) or weak (DE,
167 but low coverage and low signal-to-noise). As expected, the Pareto fronts associated with
168 Glutamatergic and GABAergic cells contain perfect markers (Fig. 1f) that identify these populations
169 with high confidence across all technologies sampled, such as *Gad1* for GABAergic cells and *Neurod2*
170 for Glutamatergic cells. In contrast, there is no perfect marker for non-neuronal cells: their Pareto
171 front only includes highly sensitive markers such as *Qk* (highly expressed in non-neurons but also
172 expressed in neurons) and highly specific markers such as the *Slco1c1* transporter (high signal-to-
173 noise, but not covering all non-neurons), consistent with the heterogeneous nature of non-neurons
174 and the need to use several markers in conjunction (Fig. 1f). Remarkably, the Pareto fronts were
175 composed of perfectly recurring genes, i.e. genes that are reliably DE across all datasets (Fig. 1e, FC >
176 4, FDR < 0.05). Conversely, this implies that markers selected based on recurrence (number of
177 datasets where they are reliably DE) naturally range from highly sensitive to highly specific. In
178 contrast, high AUROC markers have high sensitivity but low specificity.

179 To illustrate that the chosen statistics and thresholds offer an intuitive understanding of coverage
180 and signal-to-noise ratio, we plotted the expression of markers along the Glutamatergic Pareto front
181 in one of the BICCN datasets (Fig. 1g). Highly sensitive markers (*Arpp21* and *Sv2b*, AUROC > 0.8) are
182 expressed in all Glutamatergic cells at high levels but are also expressed in background cells (e.g.,
183 high expression of *Arpp21* in the *Vip*, *Sncg* and *Lamp5* cell types). The highly specific marker (*Exph5*,
184 FCd > 8) is expressed almost exclusively in glutamatergic cells, but not in all cells, indicating high
185 drop-out propensity or cell-type specific expression (e.g., it is almost not expressed in L5/6 NP).
186 Finally, the perfect markers (*Satb2* and *Neurod2*) cover almost all cells of interest and have very
187 limited background expression. To further investigate if our simple metrics capture known marker
188 genes, we investigated the Pareto fronts of inhibitory subclasses as defined by the BICCN. We found
189 that all classical markers were on the Pareto front (Sup. Fig. 1h), classified as perfect markers (*Pvalb*,
190 *Lamp5*) or highly sensitive markers (*Sst*, *Vip*), with the notable exception of *Sncg*, which was only

191 imperfectly detected in most datasets (low coverage, high signal-to-noise). A look at the Pareto front
192 of the *Sncg* population suggests that multiple genes would offer better coverage than *Sncg* while
193 preserving a high signal-to-noise ratio, in particular *Cadps2*, *Frem1* and *Megf10* (Sup. Fig. 1i), but
194 that all markers tend to have some background expression in the *Vip Serpinf1* cell type. For
195 Glutamatergic subclasses, the Pareto fronts suggested that all subclasses have perfect markers,
196 except for IT subclasses, consistent with previous observations of gradient-like properties (Tasic et
197 al. 2018; Yao et al. 2020a, 2020b) (Sup. Fig. 1j,k).

198 The FC/AUROC plot rapidly informs about the maximal strength of markers that can be expected for
199 any given cell type. In contrast to the Volcano plot, which is based on one effect size and one
200 significance statistic (Goedhart and Luijsterburg 2020), it relies on two effect sizes. Because we
201 obtain replicable statistics by combining values over multiple datasets, we remove the need to
202 visualize significance and obtain a plot with two interpretable dimensions of marker strength: signal-
203 to-noise ratio and coverage. Typically, for each population, we suggest building the FC/AUROC plot
204 across at least 5 datasets, identify genes on or next to the Pareto front, visualize their expression
205 across datasets to appreciate the optimal coverage/signal-to-noise trade-off, then select the best
206 marker(s) for the application at hand.

207 The strength of individual markers decreases with finer cell type resolutions

208 The BICCN defined three levels of cell types: classes (such as glutamatergic neurons), subclasses
209 (such as PV+ interneurons), and clusters (such as Chandelier cells)(Fig. 2a). While classes and
210 subclasses had been previously experimentally characterized and showed strong statistical
211 robustness across datasets, clusters obtained from independent datasets were more elusive (Yao et
212 al. 2020a). To further characterize how distinct cell types are, we evaluated the number of replicable
213 markers with increasing clustering resolution. We controlled for the increasing number of cell types
214 by using a hierarchical approach, for example we compare a cluster to clusters from the same
215 subclass only (Fig. 2a).

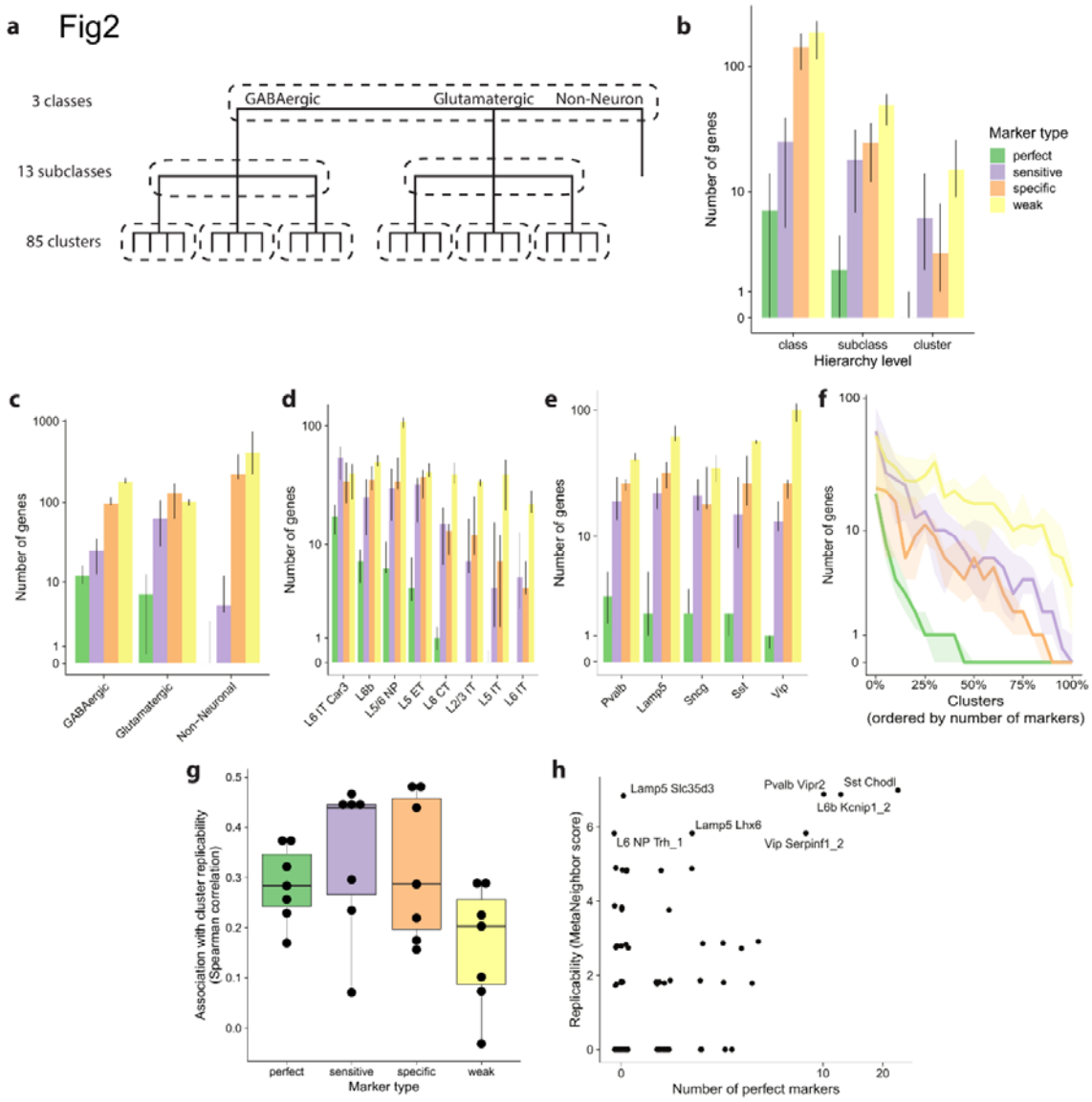

Figure 2. Markers are associated with higher cluster replicability, but become rare at finer resolutions. a *Schematic of the BICCN taxonomy. Markers are selected hierarchically: each cluster is only compared to its direct neighbors in the hierarchy (dashed lines).* ***b*** *Number of reliable markers (FC>4, FDR<0.05) along the BICCN cell type hierarchy, according to marker type: perfect (AUROC > 0.8 and FCd > 8), specific (AUROC > 0.8), sensitive (FCd > 8) and weak (FDR < 0.05).* ***c*** *Number of markers of each type for BICCN classes, error bars are interquartile range across datasets.* ***d*** *Same as c for Glutamatergic subclasses.* ***e*** *Same as c for GABAergic subclasses.* ***f*** *Number of markers of each type for BICCN clusters, with cell types ordered according to number of markers. Ribbons indicate interquartile range across datasets.* ***g*** *Association between number of makers and cross-dataset MetaNeighbor replicability score at the cluster level (Spearman correlation, one dot per BICCN dataset).* ***h*** *Illustration of association of replicability (MetaNeighbor score) and number of markers in the scCv2 dataset.*

To investigate how the number and quality of markers depends on the cell type hierarchy, we extracted all reliable markers (FC>4, FDR<0.05) and classified them as perfect (AUROC > 0.8 and FCd > 8), specific (AUROC > 0.8), sensitive (FCd > 8) and weak (FDR < 0.05). We observed an overall decrease in the median number of markers when going from coarse to finer resolution (397 total

231 markers at the class level, 108 at the subclass level, 35 at the cluster level), confirming that the signal
232 that separates neighboring populations becomes increasingly weaker (Fig. 2b). We found that all
233 classes and subclasses had at least one perfect marker except for non-neurons and IT subclasses (Fig.
234 2b-e). In contrast, only around 50% of clusters had a perfect marker (Fig. 2f, Sup. Fig. 2a-d). This
235 proportion dropped to 25% with the additional requirement that the marker should be robust across
236 all technologies (Sup. Fig. 2a). Strikingly, a handful of clusters had extremely strong support, totaling
237 close to 50 perfect markers in some of the datasets. Upon closer investigation, these clusters
238 corresponded to experimentally identified populations, such as the long-projecting interneurons
239 (Tasic et al. 2018; Paul et al. 2017)(*Sst Chodl*, up to 43 perfect markers) or Chandelier cells (Paul et al.
240 2017; Tasic et al. 2018)(*Pvalb Vipr2*, up to 20 perfect markers), suggesting that for these cell types,
241 experimentally characterized differences in morphology and physiology are reflected by a high
242 number of marker genes. Reassuringly, almost all clusters had at least one specific marker,
243 suggesting the presence of unique characteristics (Fig. 2f, Sup. Fig. 2b).

244 While more data are needed to experimentally validate cell types, we wondered whether the
245 number of markers would be predictive of computational replicability. Intuitively, a higher number
246 of markers indicates unique aspects in a population's transcriptional program, which should increase
247 its identifiability across datasets. We assessed cluster replicability using MetaNeighbor, which tests
248 the consistency of cell types across datasets using a neighbor voting framework: intuitively, if two
249 clusters represent the same cell type, they will preferentially vote for each other (see Materials and
250 Methods). We found that cluster replicability was indeed associated with the number of markers
251 (rho=0.4, Fig 2g). To understand why replicability and number of markers are only partially
252 associated, we further investigated the relationship in the best-powered datasets. We noted that,
253 while a high number of markers was associated with higher replicability, a low number of markers
254 did not imply low replicability (Fig 2h). Some clusters, such as *Lamp5 Slc35d3*, are found
255 independently in all BICCN datasets and match with high statistical confidence (MetaNeighbor
256 replicability > 0.7), despite the absence of strong markers. However, we noted that these clusters

usually had a high number of specific markers (Sup. Fig. 2e). Conversely, we found some instances of clusters with low replicability and high number of markers (e.g. *Pvalb Nkx2.1*, Sup. Fig. 2f) but, upon further investigation, all identified "markers" were stress-related genes likely to be artefacts of the extraction protocol. Overall, the imperfect association of markers and replicability suggests that individual markers only provide a partial view of cell type identity, which is encoded broadly across the transcriptome.

Meta-marker aggregation enables near-optimal cell type descriptions

Our previous results suggest that, at the finest level of resolution, single markers are not sufficient to unambiguously identify cell types (only ~10 genes with AUROC > 0.8 at the subclass level, Fig. 3a). These results are consistent with the ideas that markers are affected by dropout and that clustering procedures capture information from the full transcriptome. We next tested if cell type identity can be efficiently characterized by redundant marker lists. In particular, we ask how many markers contribute to make cell types more unique, and how the selection of replicable markers improves cell type characterization.

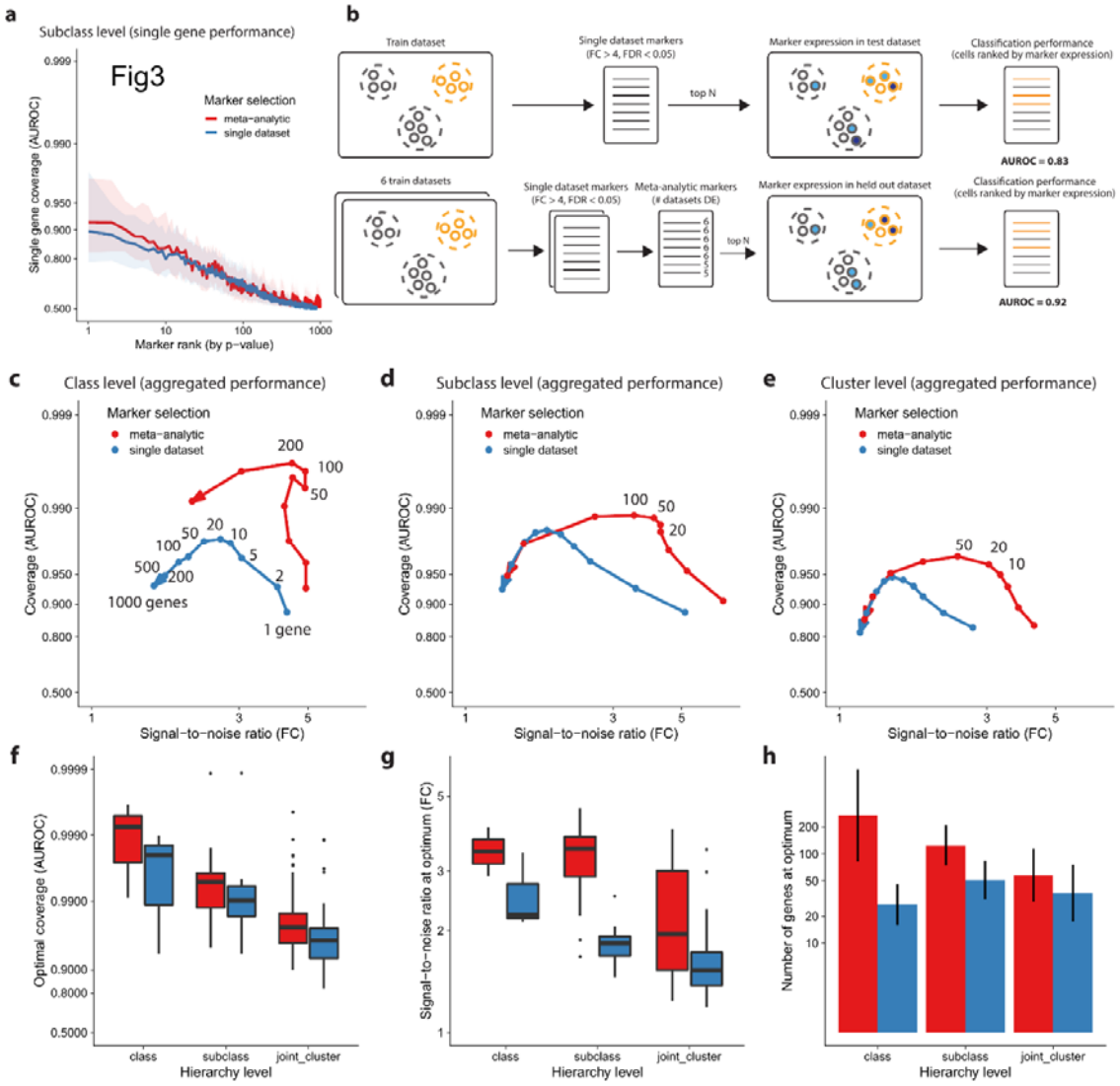

271

272 ***Figure 3. Meta-analytic aggregation of markers considerably improves the coverage/signal-to-noise trade-off. a*** *Cell type*
273 *classification performance of single markers as a function of marker rank.* ***b*** *Schematic of classification task using cross-*
274 *dataset validation for markers from single datasets and meta-analytic markers.* ***c*** *Cell type classification performance of*
275 *aggregated markers (average expression) with increasing number of markers. Performance is plotted as a parametric curve*
276 *in a coverage (AUROC), signal-to-noise (fold change) space similar to Figure 1. The arrow points toward an increasing*
277 *number of markers, the numbers next to the dots show the number of genes at which performance was measured (shown*
278 *in full as an example for one arrow, otherwise highlighting optimal performance).* ***d*** *Same as c at the subclass level.* ***e*** *Same*
279 *as b at the cluster level.* ***f-h*** *Coverage (f), signal-to-noise ratio (g) and average number of genes (h) at optimal coverage as a*
280 *function of hierarchy level. Boxplots show median and interquartile range (f,g), bar plot shows mean and standard*
281 *deviation (h) across datasets. In all panels, colors indicate whether markers were prioritized according to a single dataset or*
282 *using the meta-analytic approach.*

283 To study how the number of markers affects cell type identifiability, we framed gene aggregation as

284 a classification task (Fig. 3b). How well can we predict cell type identity for the average expression of

285 an increasing number of markers? We first created ranked marker lists for each dataset by ranking

286 genes according to their AUROC. To test the effect of meta-analytic marker selection, we used cross-

287 dataset validation: we computed marker replicability across 6 datasets and predicted cell types on
288 the held-out dataset. To rank meta-analytic markers, we used two criteria: first, the number of
289 datasets in which they were reliable DE (FC>4, FDR<0.05), second, the average AUROC. To predict
290 cells that belong to a given cell type, we ranked cells based on the average expression of the top N
291 markers for that cell type. We visualized performance in the FC/AUROC space, displaying
292 classification results as a trade-off between coverage (AUROC) and signal-to-noise ratio (FC). We
293 found that marker aggregation improved cell type identification at all levels of the hierarchy,
294 independently of the marker prioritization strategy (Fig. 3c-e). Coverage reached an optimum
295 between 10 and 200 genes (Fig. 3c-e), at the cost of a slightly lower signal-to-noise ratio (class, FC=6
296 to 6, subclass, 6 to 5, cluster, 5 to 3). Optimal performance was reached between 50 and 200 genes
297 for classes, 20 to 100 genes for subclasses, and 10 to 50 genes for clusters.

298 Meta-analytic markers systematically outperformed single dataset marker genes in terms of
299 coverage (Fig. 3f, class, AUROC=0.92 to 0.99, subclass, 0.9 to 0.99, cluster 0.85 to 0.95), signal-to-
300 noise ratio (Fig. 3g) and number of relevant genes (Fig. 3h). In other words, the best candidates in a
301 single dataset by a single metric are "too good to be true". The gain in signal-to-noise ratio is
302 particularly apparent at the cluster and subclass levels (Fig 3d-e), suggesting that the meta-analytic
303 approach successfully extracts and combines lowly expressed markers. We checked that all results
304 were robust to another marker prioritization strategy, where we ranked genes by fold change
305 instead of AUROC (Sup. Fig. 3a-c).

306 We further investigated how the performance was distributed within hierarchy levels and across
307 datasets (Sup. Fig. 3d-o). The overall classification performance (AUROC) increased with dataset
308 depth (Sup. Fig. 3d). More surprisingly, the signal-to-noise ratio was approximately constant across
309 datasets (Sup. Fig. 3h) and the number of relevant markers was slightly lower for high depth
310 datasets (Sup. Fig. 3l). Classification performance was high for all classes and subclasses (median
311 AUROC > 0.99, median FC > 3, Sup. Fig. 3e,f,i,j), with the notable exception of L5 IT and L6 IT (AUROC

312 < 0.99, FC < 3). The classification performance had a wide variance at the cluster level (AUROC
313 ranging from 0.9 to 1, FC ranging from 1.5 to 8, Sup. Fig. 3g,k), 32/85 cell types had a low signal-to-
314 noise ratio (median FC < 2, Sup. Fig. 3g). Finally, we found that the ideal number of markers ranged
315 from 10 to 200 and was remarkably consistent within each hierarchy level (Sup. Fig. 3l-o).

316 Meta-marker enrichment is robust across datasets

317 Automatic annotation of cell types typically involves two steps: (a) prioritize cells that are most likely
318 to belong to a given cell type, (b) annotate cells that exceed a pre-specified threshold condition. The
319 threshold indicates that there is enough evidence to proceed with the annotation, for example
320 preventing misannotation when a cell type is missing in the reference dataset. In the previous
321 assessment, we showed that meta-analytic marker lists successfully prioritize cells, without explicit
322 consideration for correct thresholding. We wondered whether marker expression was sufficiently
323 consistent to be compatible with a simple thresholding method: a cell belongs to a given cell type
324 when its marker expression exceeds the same pre-specified value for each test dataset.

325 For each dataset in the compendium, we computed the annotation performance at various
326 threshold values (Fig. 4a). For example, in the *Pvalb* subclass, meta-analytic markers had a high
327 maximal performance (F1opt>0.9) across all datasets (Fig. 4c). Additionally, the maximal
328 performance had a distinctive plateau, indicating that a large range of thresholds had almost
329 equivalent performance, as expected from the meta-markers' tendency to preserve a high signal-to-
330 noise ratio. To visualize how well optimal thresholds aligned across datasets, we defined the
331 plateauing region as the thresholds that had at least 90% of the maximal performance (Fig. 4b).
332 While there was a large plateau in all datasets, the plateaus did not align well, suggesting
333 normalization issues (Fig. 4c). As a result, a meta-analytic threshold leads to good performance in
334 most datasets, but fails in dataset with extreme properties, such as snCv2 (nuclei, 10X v2, low depth)
335 or scCv3 (cells, 10X v3, high depth).

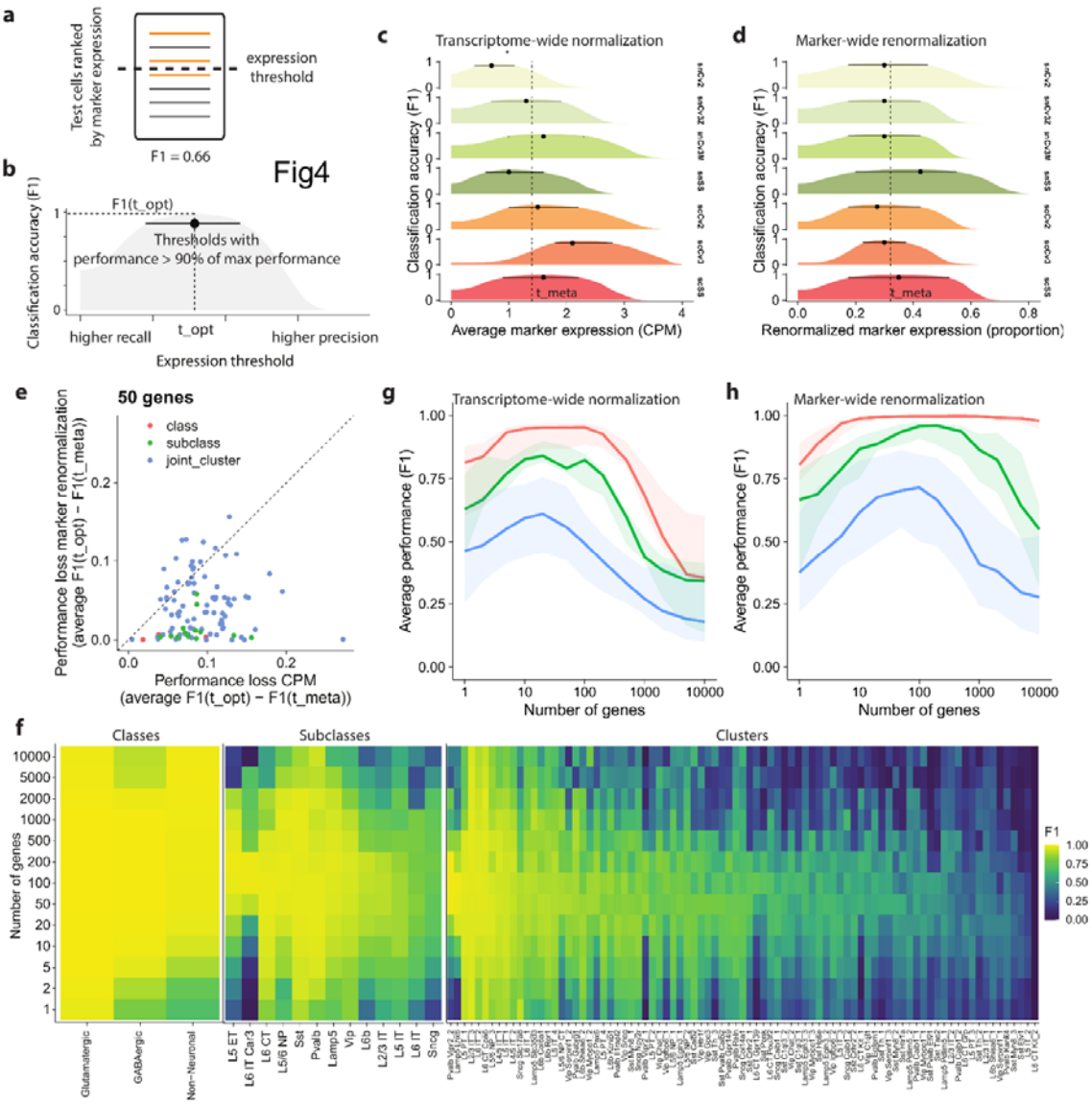

336

337 ***Figure 4. Aggregated expression of meta-analytic markers enables robust identification of cell types. a*** *Schematic of*
338 *threshold-based classification. The initial steps of the procedure are identical to Figure 3.* ***b*** *Illustration of statistics*
339 *measuring cell type annotation performance at various thresholds. For a given dataset, cell type and number of genes (scSS*
340 *dataset, Pvalb subclass, 100 genes in the illustration), F1opt is the score obtained by picking the single best threshold,*
341 *indicated by a dot. The line indicates the range of near-optimal thresholds (leading to a performance higher than*
342 *0.9*F1opt).* ***c*** *Comparison of near-optimal expression thresholds across datasets (for Pvalb subclass and 100 genes). The*
343 *position of the dotted line (F1meta) is obtained by averaging optimal expression thresholds across datasets.* ***d*** *Similar to b,*
344 *but defining optimal thresholds based on proportion of marker expression instead of expression.* ***e*** *For each cell type, we*
345 *show how much performance is lost by switching from a dataset-specific threshold (F1opt) to a single meta-analytic*
346 *threshold (F1meta) for the two types of thresholds (CPM expression, marker expression proportion). Colors indicate*
347 *hierarchy level, the dashed line is the identity line (performance loss is identical for the two types of thresholds).* ***f*** *For each*
348 *hierarchy level, heatmap detailing classification performance for each cell type as a function of the number of genes.* ***g-h***
349 *Average performance as a function of the number of genes using the optimal meta-analytic expression threshold (g) or*
350 *optimal marker expression proportion threshold (h). Ribbons show interquartile range across populations and test datasets.*

351 To overcome the normalization discordance, we reasoned that the normalization issues are mainly

352 driven by non-marker genes. Instead of considering marker expression for each cell type

353 independently, we divided marker expression by the total marker expression (across all putative cell
354 types). After this change, plateaus of optimal thresholds aligned across all datasets (Fig. 4d),
355 suggesting that marker lists have preserved relative contributions in all datasets. To assess the utility
356 of marker-wide renormalization, we directly compare how much performance is lost by switching
357 from dataset-specific thresholds (optimal threshold per dataset) to a consensus threshold. The
358 decrease in performance was systematically lower with marker-wide renormalization for classes and
359 subclasses and was generally lower for clusters (Fig. 4e).

360 We compared the performance achieved for transcriptome-wide and marker-wide normalization as
361 a function of the number of markers (Fig. 4g-h, Sup. Fig. 4a-b) and within each hierarchical level (Fig.
362 4f, Sup. Fig. 4c-e). Both methods reached high classification performance at the class and subclass
363 level (optimal average F1 > 0.75, Fig. 4g-h), but the average performance was considerably lower at
364 the cluster level. Marker-wide normalization yielded substantially higher classification performance
365 (ΔF1 ~ 0.1) and reached peak performance by successfully integrating a higher number of genes (50-
366 500 markers, Fig. 4g-h). Performance was distributed unequally within hierarchy level, in particular
367 for subclasses and clusters (Fig. 4f). Almost all subclasses reached optimal performance around 100-
368 200 markers with a high performance (F1 > 0.75), with the exception of L5 IT, L6 IT and *Sncg*. At the
369 cluster level, the performance degraded substantially: peak performance was attained around 50-
370 100 markers, with only 43/85 of cell types reaching high performance (F1 > 0.75). All these trends
371 were consistent with results obtained using transcriptome-wide normalization, with overall higher
372 annotation performance (Sup. Fig. 4c-e).

373 Meta-markers are enriched for genes involved in synaptic regulation and 374 development

375 We next wondered if top meta-markers were enriched for specific biological processes. We
376 performed gene set enrichment analysis for the top markers in each cell type against Gene Ontology

(GO) terms from the Biological Process (BP) ontology. To focus on specific processes, we only queried terms containing between 20 and 100 genes. For each cell type, we extracted the top 3 enriched terms based on the False Discovery Rate (FDR) from the hypergeometric test. The best balance between number of enriched terms and cell type specificity was achieved for the top 100 markers for both classes and subclasses (Fig. 5a, Sup. Fig. 5a).

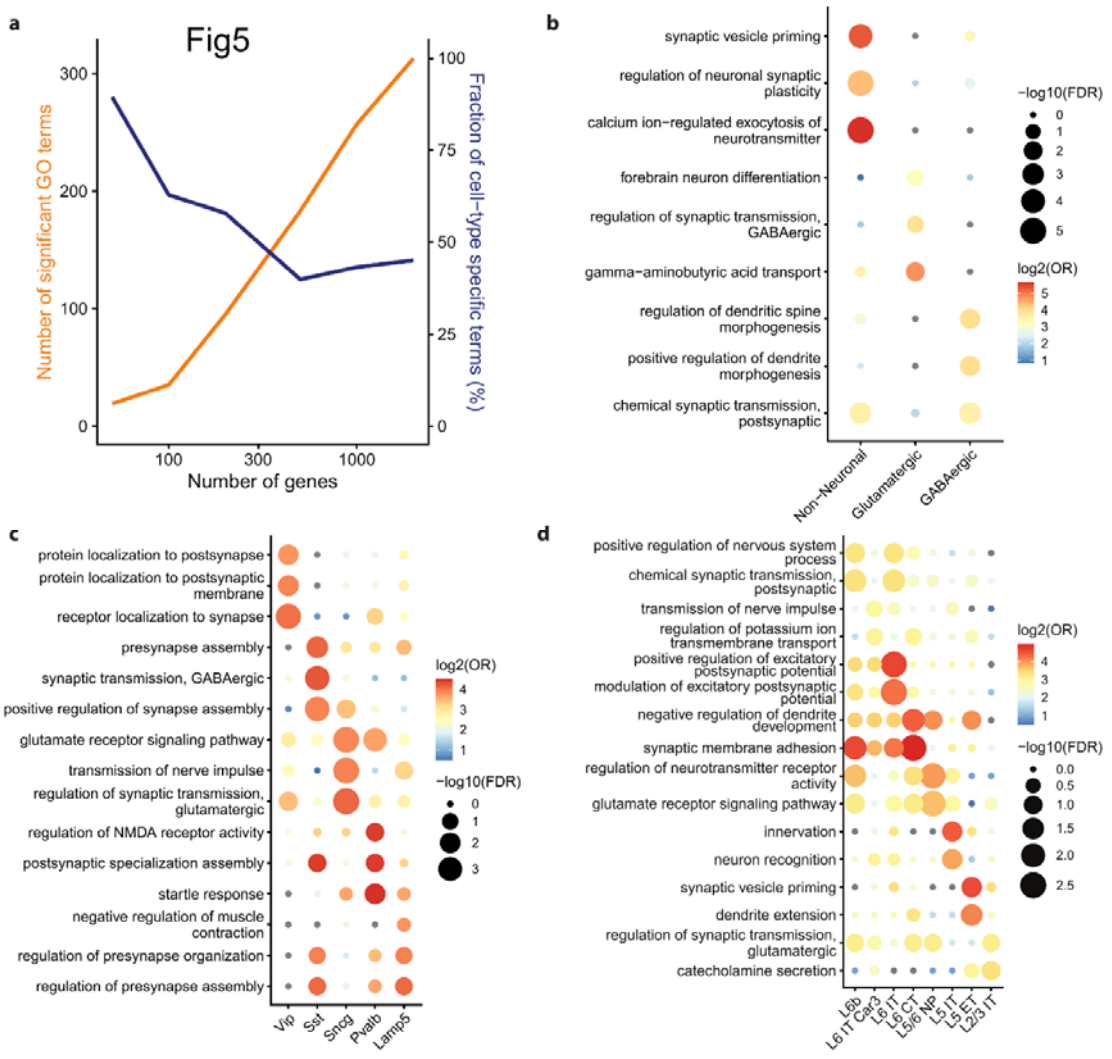

Figure 5. The top 100 meta-markers are enriched for specific synaptic processes. a *Total number of significantly enriched GO terms (orange) and fraction of significant GO terms that are enriched in a unique cell type (blue) for BICCN subclasses when an increasing number of meta-markers are considered.* ***b*** *Top 3 enriched Gene Ontology (GO) terms for the top 100 meta-markers for each BICCN class. For each dot, the size reflects the False Discovery Rate (FDR), the color reflects the Odds Ratio (OR) of the enrichment test (hypergeometric test).* ***c*** *Same as* ***b*** *for the top 100 meta-markers for BICCN GABAergic subclasses.* ***d*** *Same as* ***b*** *for the top 100 meta-markers for BICCN Glutamatergic subclasses (only top 2 terms per cell type are shown).*

390 We found strong enrichment for synaptic properties for all cell types. At the class level, non-
391 neuronal markers were enriched for synaptic support functions, such as "Regulation of neuronal
392 synaptic plasticity" (Fig. 5b). Glutamatergic neurons were enriched for synaptic regulation (such as
393 the regulation of GABAergic transport), while GABAergic neurons were enriched for gene sets
394 related to the regulation of spine and dendrite formation. At the subclass level (Fig. 5c,d), GABAergic
395 neurons were most distinguishable based on synaptic sub-properties, such as localization to synapse
396 (*Vip*), synapse assembly (*Sst*, *Lamp5*), or glutamate transmission regulation (*Sncg*). Glutamatergic
397 subclasses showed a similar enrichment of synaptic sub-properties, including various aspects of
398 potential regulation and synaptic transmission (L6b, L6 IT, L2/3 IT, L5/6 NP), as well as synaptic
399 development (L6 CT, L5 IT, L5 ET). We further confirmed that these findings were consistent with the
400 enrichment of the top 200 markers, which also highlighted gene sets involved in synaptic regulation
401 and development (Sup. Fig. 5b-d). These results suggest that meta-markers define a plausible
402 biological subspace revealing cell type differences in terms of synaptic properties.

403 Meta-markers improve deconvolution performance

404 One of the primary purposes to which cell atlas data may eventually be put is deconvolution of bulk
405 data where cell composition is likely related to the condition of interest (e.g., disease). Single cell
406 data have been routinely used to increase deconvolution performance in recently developed tools
407 (Tsoucas et al. 2019; Wang et al. 2019; Newman et al. 2019; Dong et al.), but performance remains
408 plagued by batch effects and cell type similarity (Newman et al. 2019; Huang et al. 2020; Cobos et al.
409 2020). The role of marker genes in deconvolution remains particularly unclear: a recent benchmark
410 suggests that the quality of markers is more important than the deconvolution method (Cobos et al.
411 2020), in most studies the influence of the number of markers is only partially assessed (Newman et
412 al. 2019; Hunt and Gagnon-Bartsch 2019). Our annotation assessment suggested that cell types are
413 best captured with 10 to 200 meta-analytic markers; deconvolution is a natural place to test this
414 heuristic.

415 To measure the number of genes that yield maximal deconvolution performance, we generated
416 thousands of pseudo-bulk datasets with known mixing proportions from each of the BICCN datasets
417 (Sup. Fig. 6a). As in previous experiments, we directly compared the performance of markers
418 extracted from single datasets and performance of meta-analytic markers. We initially compared
419 two tasks: (a) within-dataset cross-validation, where cell type profiles are learned from a training
420 fold and tested on a held-out set from the same dataset, (b) cross-dataset-validation, where profiles
421 are learned on one dataset and tested in another dataset. Within-dataset cross-validation proved to
422 be a simple task, yielding extremely high performance (Pearson ~ 1, not shown). In contrast, cross-
423 dataset-validation showed only modest performance (Pearson ranging from 0 to 1, Sup. Fig. 6b),
424 highlighting the difficulty of the deconvolution task. Because deconvolution applications typically
425 involve different datasets, we focused our analyses on cross-dataset validation.

426 Deconvolution performance rapidly degraded along the neuron hierarchy (Sup. Fig. 6b), ranging
427 from almost perfect performance for classes (Pearson ~ 1) to low performance for clusters (Pearson
428 < 0.5). Classes were easily learnable across all tasks (Sup. Fig. 6c), even using random genes,
429 suggesting that at this level of the hierarchy, cell types are strongly uncorrelated and can easily be
430 separated along the first principal component. At the subclass level, the performance of random
431 genes remained close to 0, suggesting stronger covariation compared to classes (Sup. Fig. 6d). Meta-
432 analytic markers yielded more robust deconvolution performance, with performance increasing up
433 to 100 genes, while markers from single datasets prioritized only around 10 informative genes. The
434 trend was similar at the cluster level, but with lower overall performance (Sup. Fig. 6e). Meta-
435 analytic markers again proved to be more robust, prioritizing around 50 informative genes compared
436 to 10-20 from single datasets. Overall, our results suggest that, in conjunction with batch effects, the
437 increasing covariation of cell types at finer resolution significantly complicates the deconvolution
438 task. The prioritization of a large number of robust marker genes is an important first step towards
439 successful deconvolution.

440 ## Meta-markers reveal a generalizable description of cell types

441 We have previously shown that meta-marker signatures generalize across laboratories and
442 technologies. We next asked how well they generalize across the cortex by predicting cell types in a
443 BICCN dataset combining multiple cortical and hippocampal brain regions (Yao et al. 2020b). To
444 understand how easily meta-markers generalize, we used a straightforward annotation method:
445 assign cells to the cell type with the highest average meta-marker expression. For simplicity, we
446 considered the same number of meta-markers for all cell types: 100 at the class and subclass level,
447 50 at the cluster level.

448 We started by predicting cell types in the auditory cortex sub-dataset, containing 71,670 cells
449 annotated to 203 cell types. We chose to focus on the auditory cortex because of its large number of
450 cells, and to investigate the generalizability of cell types derived from a motor area (MOp) to a
451 sensory area. While inhibitory cell types are expected to generalize, excitatory cell types have been
452 shown to have divergent patterns (Tasic et al. 2018). At the class level, top meta-markers enabled
453 perfect classification down to every single cell (Fig. 6a). Assignments can be traced back to meta-
454 marker scores, as well as individual genes (Fig. 6b). Consistent with our previous points, the
455 GABAergic score is uniformly high across all cells labeled as GABAergic. In contrast, the expression of
456 the single best marker, *Gad1*, is more variable in GABAergic cells and displays sporadic expression in
457 non-GABAergic cells.

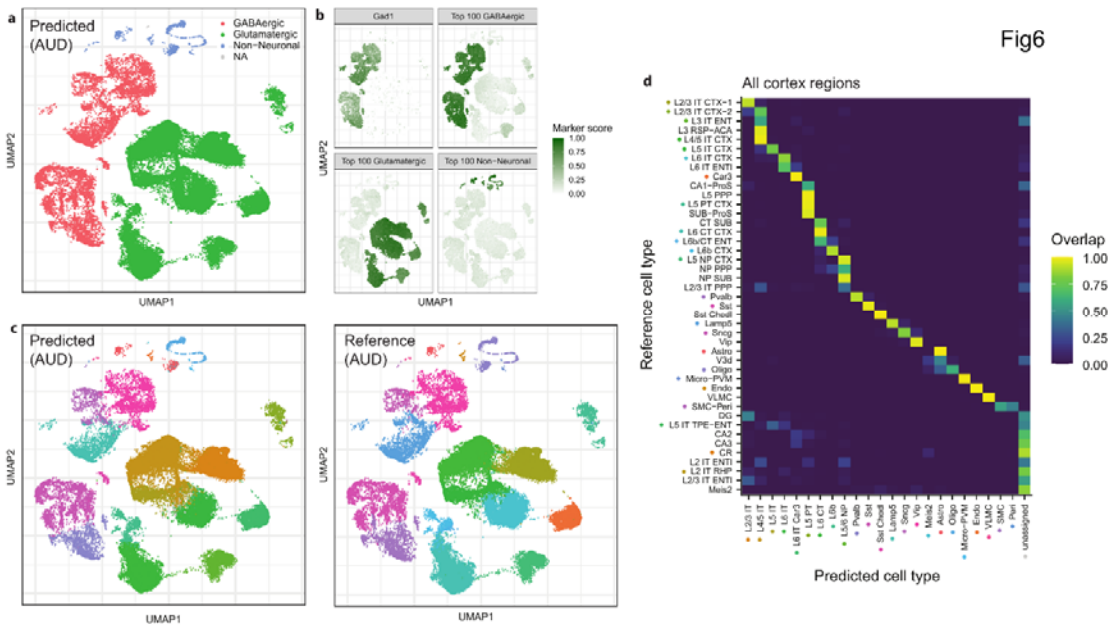

Figure 6. Meta-analytic markers from the primary motor cortex (MOp) generalize to other cortical regions. a *Example of class-level predictions in the auditory cortex (AUD), where cells are embedded in UMAP space and colored according to predictions based on the top 100 meta-markers for MOp classes. Cells are assessed independently and remain unassigned (NA) if the marker enrichment score is lower than 1.5 for all classes.* ***b*** *Marker scores (re-normalized between 0 and 1) used to determine cell type assignments. The first subpanel shows the score obtained from a single GABAergic marker, the three other panels show the scores obtained by combining the top 100 meta-markers for each class.* ***c*** *Subclass-level predictions in the auditory cortex based on the top 100 MOp meta-markers (left) and reference labels (right). Cells remain unassigned (NA) if the marker enrichment score is lower than 1.5 for all subclasses. See panel* ***d*** *for color legend (some reference cell types are absent from AUD).* ***d*** *Confusion matrix showing the concordance of subclass-level predictions based on the top 100 meta-markers with reference cell types across 40 brain areas. Cells are unassigned if the marker enrichment is lower than 1.5 for all subclasses.*

Remarkably, at the subclass level, meta-markers enabled similarly strong cell type assignments, as suggested by the uniform coloring of clusters in UMAP space (Fig. 6c). Note that the assignments occur in each cell independently, without knowledge about clusters or expression profiles of neighboring cells, highlighting the consistency of meta-marker expression. This procedure allowed the identification of rare cell types, even when only one or two cells were present in the dataset (e.g. smooth muscle cells and pericytes, Sup. Fig. 7b). The predicted assignments corresponded almost perfectly to the reference cell types (Fig. 6c). The main exception were deep layers IT cell types, in particular one group of L5 IT cells tended to be assigned as L4/5 IT or L6 IT (Sup. Fig. 7c). Finally, cluster-level predictions also proved extraordinarily consistent, with smooth transitions between cell types that mapped with auditory cortex reference annotations (Sup. Fig. 8).

480 To further highlight high-quality predictions, we quantified assignment confidence using meta-
481 marker enrichment (observed expression over expected expression) as a "QC" metric. In the
482 auditory cortex, we found that a threshold of 1.5 offered an optimal trade-off between annotation
483 recall and precision (Sup. Fig. 9a-c). Raising the threshold to 2 further selected high-confidence calls,
484 yielding higher precision for slightly lower recall. Interestingly, cells that became unassigned were
485 mostly located in regions where predictions and reference disagreed: deep IT layers, and inhibitory
486 neurons bridging medial ganglionic eminence (MGE) and caudal ganglionic eminence (CGE)
487 subclasses (Sup. Fig. 7a). Meta-marker enrichment thus offers a good proxy for prediction quality,
488 enabling to identify cells with a high-confidence cell type assignment.

489 Next, we systematically quantified the agreement of meta-marker based predictions and reference
490 annotations across all brain regions and 43 consensus subclasses. We found exceptionally good
491 agreement, with all reference subclasses mapping to exactly one predicted MOp subclass (Fig. 6d).
492 All MOp subclasses matched strongly with their "natural" counterparts in the reference dataset,
493 such as "L2/3 IT" with "L2/3 IT CTX-1". Remarkably, reference cell types absent in MOp (such as
494 hippocampal cell types) were mostly labeled as "unassigned", suggesting that meta-marker
495 signatures correctly avoid labeling unseen cell types. This trend became particularly obvious for cells
496 with marker enrichment > 2 (Sup. Fig. 9d), where all unseen cell types became "unassigned", while
497 conserving high matching scores between shared cell types.

498 Discussion

499 By assessing marker replicability across 7 datasets, we selected robust markers and identified the
500 optimal number of markers to define a cell type. We identified highly replicable markers for 85 cell
501 types from the mouse primary motor cortex (Sup. Data 1-3). This meta-analytic strategy proved
502 particularly important for rare populations and lowly expressing genes (Fig. 1). Compared to
503 previous efforts (Tasic et al. 2018; Mancarci et al. 2017; Yao et al. 2020a), we identified a high

504 number of robust markers at high cell type resolution: at the BICCN cluster level, cell types were best
505 characterized by 10-200 meta-analytic markers, a two-fold increase of reliable markers compared to
506 markers selected from single datasets (Fig. 3). Interestingly, we found that only 50% of clusters had
507 strong markers (Fig. 2), but that some of the clusters lacking strong markers (e.g. *Lamp5 Slc35d3*)
508 were consistently identified in all BICCN datasets, suggesting broad encoding of their identity and
509 highlighting the need of extended marker signatures.

510 We found that the simple aggregation of marker expression enabled the annotation of individual
511 cells (Fig. 4), suggesting that careful feature selection is enough to provide a rough definition of cell
512 types. Remarkably, marker lists derived from a single cortical region generalized with high accuracy
513 to other cortical regions without any methodological fine-tuning (Fig. 5). By introducing redundant
514 information about cell types, meta-analytic markers dramatically increased cell type separability (Fig.
515 3). However, adding more markers is only beneficial if they are cell type-specific. As a result, we
516 established that the ideal number of markers decreases with cell type resolution: 200 genes to
517 separate classes (lowest resolution, e.g. GABAergic neurons), 100 genes for subclasses (e.g., *Pvalb*
518 interneurons) and 50 genes for clusters (highest resolution, e.g., Chandelier cells).

519 By combining datasets that were generated using different technologies, the markers we propose
520 are likely to generalize well with respect to this axis of variation. Moreover, we show that our
521 marker descriptions generalize to other cortical regions, despite all "training" datasets sampling
522 from the same cortical region. However, the data used in this study were obtained from adult mice
523 with limited genetic background and grown in lab conditions. As a result, it remains unclear how well
524 the marker descriptions would generalize across development or biological conditions. On the other
525 hand, as our approach relies on a simple procedure, marker lists can easily be extended to
526 incorporate new sources of variation, such as additional brain regions, species or biological
527 conditions. On a similar note, markers depend on one particular annotation effort, but we can
528 expect the neuron taxonomy to evolve with additional data, in particular the fine-resolution clusters.

529 Our framework, available as an R package, allows to rapidly evaluate the consistency of marker
530 expression for new cell type annotations.

531 To highlight the replicability of marker descriptions, the manuscript relies on simple methods, but
532 marker lists can easily be combined with more sophisticated methods for marker selection or cell
533 type assignment. For example, experimental applications routinely require either a few specific
534 markers to target one cell type (Huang 2014) or a panel of hundreds of markers to jointly separate
535 all cell types (Moffitt et al. 2018). Marker lists can be combined with methods to select concise sets
536 of markers (Asp et al. 2019; Zhang et al. 2020; Dumitrascu et al. 2019) by filtering candidates that
537 are likely to generalize. Similarly, development studies (Hobert 2008; Huang 2014; Kessaris et al.
538 2014; Lodato and Arlotta 2015; Mayer et al. 2018; Tosches et al. 2018) indicate that neural lineages
539 are marked by the specific onset and offset of key transcription factors (TFs), but the expression of
540 these key TFs may not be maintained at later stages or only at low levels. Since our approach is
541 powered to identify lowly expressed markers, it can be combined with time series data to help
542 identify replicable lineage-specific genes.

543 This study focused on the neuron hierarchy, but our strategy generalizes to other tissues. In order to
544 encourage broader adoption, we have made our code available as a package and in the vignette we
545 show how our analyses and guidelines can be similarly applied to a pancreas compendium. We
546 chose to focus on the BICCN dataset because of its complexity (85 neuronal cell types),
547 comprehensiveness (~500,000 cells with latest sequencing technologies) and diversity (6
548 technologies used). Our results suggest that, in the brain, there is a clear separation at the top two
549 levels of the hierarchy (3 classes, 13 subclasses), but that the molecular signature of half the clusters
550 remains unclear. We expect that similar conclusions can be drawn for other tissues, such as blood,
551 where there is a similar hierarchical organization of cell types. The main difficulty is to identify
552 replicable cell types across datasets, which may be challenging during development or complex
553 differentiation processes, such as hematopoiesis.

554 The selection of replicable markers from single cell atlases is a promising avenue for several
555 applications, including cell type annotation, selection of gene panels and bulk data deconvolution. It
556 reduces rich information to a prioritized list that is simple to use and to refine. New computational
557 methods will benefit from highly condensed prior information about genes in the cell type space,
558 without having to train on large reference datasets. Finally, as new datasets are generated, marker
559 lists will become increasingly robust to new sources of variation, leading to higher downstream
560 performance across a diverse array of tasks.

561 Materials and Methods

562 Datasets

563 We downloaded the mouse primary cortex (MOp) BICCN datasets and cell type annotations from the
564 NeMO archive (http://data.nemoarchive.org) according to preprint instructions (Yao et al. 2020a).
565 We considered the 7 transcriptomic datasets from the mouse primary cortex: single cell Smart-Seq
566 (scSS), single nucleus Smart-Seq (snSS), single cell Chromium v2 (scCv2), single nucleus Chromium v2
567 (snCv2), single cell Chromium v3 (scCv3), single nucleus Chromium v3 from the Macosko and Zeng
568 labs (scCv3M and scCv3Z, respectively)(Table 1). We kept all cells with "class" annotated as
569 "Glutamatergic", "GABAergic" or "Non-Neuronal" and kept genes that were common to all datasets,
570 arriving at a total of 482,712 cells and 24,140 genes. We normalized counts to counts per millions
571 (CPM). For cell types, we considered five levels of annotations provided by the BICCN: "class",
572 "subclass", "cluster", "joint_subclass" and "joint_cluster". "subclass" and "cluster" labels were
573 obtained by clustering and annotating the datasets independently, while "joint_subclass" and
574 "joint_cluster" labels were obtained through joint clustering and annotation. Throughout the
575 manuscript, we use "joint_cluster" labels when we need common annotations across datasets,
576 otherwise, we use "cluster" labels. To map "subclass" labels across datasets, we used the
577 independent clustering, but mapped all clusters to one of the following names: "L2/3 IT", "L5 ET",

578 “L5 IT”, “L5/6 NP”, “L6 CT”, “L6 IT”, “L6 IT Car3”, “L6b”, “*Lamp5*”, “*Pvalb*”, “*Sncg*”, “*Sst*”, “*Vip*”. In the
579 last section (generalizability of meta-markers), we use the “joint_subclass” annotation instead,
580 because it explicitly includes the distinction between L4/5 IT and L5 IT cells.

581 The BICCN isocortex and hippocampus dataset was downloaded from the NeMO archive
582 (http://data.nemoarchive.org)(Yao et al. 2020b). The full dataset contains 1,646,439 cells annotated
583 to 379 cell types. Due its size, it was separated into sub-datasets corresponding to individually
584 sequenced brain regions (as annotated in the “region_label” metadata column), resulting in 19 brain
585 regions sequenced with 10X v3, 21 brain regions sequenced with SmartSeq (Table 1). We subset all
586 datasets to a common set of 24,140 genes. Preprocessing was similar to the MOp datasets: we kept
587 all cells with “class” annotated as “Glutamatergic”, “GABAergic” or “Non-Neuronal” and normalized
588 counts to counts per million (CPM) for SmartSeq datasets or counts per 10,000 (CP10K) for 10X
589 datasets.

590 Meta-analytic hierarchical differential expression statistics

591 For each cell type, we computed DE statistics independently in each dataset using MetaMarkers’
592 “compute_markers” function. We compared a cell type to neighboring cell types in the BICCN
593 taxonomy by setting the “group_labels” parameter. For example, the “GABAergic” class contains the
594 “*Pvalb*”, “*Sst*”, “*Sncg*”, “*Lamp5*” and “*Vip*” subclasses. By stratifying analysis by classes, DE statistics
595 for “*Pvalb*” were obtained by comparing “*Pvalb*” cells to all cells that are either “*Sst*”, “*Sncg*”,
596 “*Lamp5*” or “*Vip*”, but ignoring cells from other classes (excitatory neurons and glia). At the cluster
597 level, analysis is stratified by subclasses, e.g., *Pvalb* subtypes are compared to other *Pvalb* subtypes
598 only.

599 For each dataset, “compute_markers” returns a table of standard statistics. Let x_{ij} be the expression
600 of gene i in cell j (normalized to CPM in all the manuscript), let C be the cells belonging to the cell
601 type of interest, and $\overline{C}$ be all background cells. All statistics are computed for each gene

independently, so we will drop the subscript i in the following. The fold change (FC) is computed as the ratio of average expression between the cell type of interest and background cells, $FC = \overline{\{x_j\}_{j\in C}} / \overline{\{x_j\}_{j\in \overline{C}}}$. Statistical significance is based on the ROC test. First we compute the AUROC according to the following formula (derived from the Mann-Whitney U statistic):

$$AUROC = \frac{1}{NP}\left(\sum_{j\in C} r_j - \frac{P(P+1)}{2}\right),$$

where $P = |C|$ are the number of positives (cells from the cell type of interest), $N = |\overline{C}|$ are the number of negatives (background cells), and r_j are the ranks of positives (obtained after ranking all cells according to the gene's expression value). P-values are computed under a normal approximation of the AUROC with continuity and tie correction according to the following formulas:

$$z = (AUROC - 0.5) / \sigma; \quad \sigma = \sqrt{\frac{NP}{12}(P + 1 - T)}; \quad T = \sum_{i=1}^{k} \frac{{t_i}^3 - t_i}{(N+P)(N+P+1)};$$

where z follows a standard normal distribution under the null hypothesis that positives and negatives are from the same population, σ is the analytical standard deviation of AUROC, T is a tie correction formula where k is the number of distinct expression values and t_i is the number of cells that share the same expression value with index i. P-values are converted to False Discovery Rates (FDR) according to the Benjamini-Hochberg procedure. For exhaustivity, we considered four additional statistics related to binarized gene expression: gene detection rate, fold change of detection rate (FCd), recall and precision. Gene detection rate is the fraction of cells in the population of interest that express the gene of interest, $dr_C = |\{x_j > 0\}_{j\in C}| / |C|$. FCd= $dr_C / dr_{\overline{C}}$ is the ratio of gene detection rates in the population of interest over the background population. Recall is identical to gene detection rate (seen from a classification perspective). Precision= $|\{x_j > 0\}_{j\in C}| / |\{x_j > 0\}_{j\in C\cup\overline{C}}|$ is the fraction of cells expressing the gene of interest that belong to the population of interest. All operations are vectorized across genes and cell types to allow rapid marker extraction and aggregation across datasets.

625 We combined statistics across datasets using MetaMarkers' "make_meta_markers" function, which
626 averages the above statistics across datasets for all cell types. "make_meta_markers" uses the
627 arithmetic mean by default, and uses the geometric mean for the following statistics: FC, FCd,
628 expression. To define DE recurrence, we used the number of datasets where a gene is reliably DE
629 ("fdr_threshold=0.05", "fc_threshold=4"). Throughout the manuscript, we considered a gene to be
630 DE if it had a FC>1 and an FDR<0.05, and reliably DE if FC>4 and FDR<0.05.

631 Reliable fold change and AUROC thresholds

632 To establish the reliability of FC, we picked all combinations of training datasets and extracted genes
633 that were significantly upregulated in all training datasets (AUROC>0.5, FDR<0.05, average FC>1).
634 Then, for each gene, we looked up the held out datasets and counted how often the gene remained
635 upregulated (FC>1) or was detected as downregulated (FC<=1). We summarized the results as a type
636 S error, the fraction of held out datasets where the gene was detected as downregulated. Formally,
637 let G be the set of genes that are consistently upregulated across training datasets d_1, ..., d_m. Let d'_1,
638 ..., d'_n be the held-out test datasets. For a given cell type, the average type S error is defined as:

639 $$e = \frac{1}{n|G|}\left|\{FC_{gd'_i} < 1\}_{g \in G, i \in \{1..n\}}\right|,$$

640 where $FC_{gd'_i}$ is the fold change of gene g in test dataset d'_i. We computed the type S error across all
641 combinations of cell types and training datasets. To establish the reliability of AUROC, we followed a
642 similar procedure, replacing the FC<1 condition by AUROC>0.5.

643 MetaNeighbor cell type replicability score

644 To compute the association between the number of markers and cell type replicability, we
645 computed cell type similarity using MetaNeighbor by following the procedure described in (Yao et al.
646 2020a). Briefly, MetaNeighbor uses a neighbor voting framework to match cell types from a train
647 dataset to a test dataset, where the matching strength is quantified as an AUROC. First, we use the

648 "MetaNeighborUS" function to create a graph where each node is a cell type and each edge is the
649 matching strength (directed from train dataset to test dataset). By applying the
650 "extractMetaClusters" function, we keep only edges that correspond to high confidence reciprocal
651 matches (1-vs-best AUROC > 0.7 both ways). After this step, we are left with groups of connected
652 cell types that we call "meta-clusters". The replicability score is the number of datasets spanned by
653 the meta-cluster, e.g. a cell type has a score of 6 if it is connected to cell types from 5 other datasets.
654 For visualization purposes, we created jittering by adding the average AUROC across the meta-
655 cluster to the replicability score. To avoid overfitting, we considered the "cluster" annotations from
656 the BICCN, which were obtained by clustering and annotating the datasets independently.

657 Marker-based cell type classification

658 To quantify the ability of a list of markers to identify a cell type, we framed the problem as a
659 hierarchical classification task where we predict cell type labels from gene expression. First, for each
660 cell, we computed a prediction score by averaging expression profiles across markers. Let x_{ij} be the
661 CPM-normalized expression of gene $i$in cell j, and M_c be a set of marker genes for cell type c. For
662 each cell j, we compute the marker score is:

$$S_j(c) = \frac{1}{|M_c|} \sum_{i \in M_c} log2(x_{ij} + 1)$$

663 This score is efficiently implemented by MetaMarker's "score_cells" function. To obtain marker-wide
664 renormalized scores, we compute the above score for a series of cell types $c_1, .., c_n$ then, for each
665 cell type, we compute:

$$S'_j(c) = S_j(c) \,/\, \frac{1}{n} \sum_{i=1}^{n} S_j(c_i)$$

666 To compute classification performance, we labeled cells from the cell type of interest as positives
667 and cells from cell types sharing the same parent class or subclass as negatives (similar to DE

statistics computation, see “Meta-analytic hierarchical differential expression statistics”). Intuitively, we are looking whether positives (cells from the cell type of interest) have high prediction scores (marker scores). We summarized the prediction accuracy as an AUROC (in the threshold-free case) and F1 (harmonic mean of precision and recall, in the thresholding case). To avoid circularity, we always made predictions on held out datasets. For markers from a single dataset, predictions were averaged across the 6 remaining datasets; for meta-analytic markers, we picked markers on all combinations of 6 datasets and predicted cell types in the remaining dataset. We obtained classification scores for individual populations of neurons by averaging over every combination of train and test datasets.

Gene ontology enrichment of meta-markers

Gene ontology terms and mouse annotations were downloaded using the org.Mm.eg.db and GO.db R packages. To focus on specific cell processes, we further selected terms from the “Biological Process” ontology containing between 20 and 100 gene annotations. Gene set enrichment was computed using the hypergeometric test, based on R’s “phyper” function and the Maximum Likelihood Estimate (MLE) of the sample odds ratio (OR).

Marker-based deconvolution

To investigate the impact of marker selection on deconvolution, we applied deconvolution in a hierarchical framework similar to DE computation and cell type classification. We applied Non-Negative Least Square (NNLS) deconvolution (Abbas et al. 2009) using the nnls R package, which was shown to be both efficient and accurate according to multiple recent benchmarks (Patrick et al. 2020; Cobos et al. 2020). Briefly, we inferred cell type proportions from the following equation:

$$T = C.P$$

where T is a bulk expression matrix (genes x sample), in our case pseudo-bulk matrices extracted from each test dataset, C is a cell type signature matrix (genes x cell type), P is the estimated cell

691 type proportion matrix (cell type x sample). To test all combinations of train and test datasets, we
692 split each dataset in half by assigning each cell randomly to a test or train fold. From each train fold,
693 we built signature matrices by averaging unnormalized expression profiles for each cell type. From
694 each test fold, we built 1000 pseudo-bulks containing 1000 cells. To generate pseudo-bulks with
695 highly variable cell type proportions, we started by drawing target cell type proportions for each
696 pseudo-bulk, in a procedure similar to (Cobos et al. 2020). We sampled target proportions for each
697 cell type from a uniform distribution, normalized proportions to 1, then converted to a target
698 number of cells which we sampled with replacement, then averaged the unnormalized counts.

699 Given a set of markers (obtained from a single dataset or meta-analytically across all datasets except
700 the test dataset), a train dataset (signature matrix) and a test dataset (1000 pseudo-bulks), we
701 performed NNLS deconvolution by subsetting the signature matrix C and pseudo-bulks T to the set of
702 markers. We computed deconvolution performance as the Pearson correlation between theoretical
703 cell type proportions and the predicted cell type proportions (one value per pseudo-bulk). For
704 computational efficiency, we only tested one group of populations at the "joint cluster" level. We
705 chose to focus on the Lamp5 populations, as it contained 8 populations that were well represented
706 across all datasets (range 14 to 3016 cells per single population, 257 cells on average).

707 Note that, because of the difficulty of matching UMI counts with full-length read counts (Newman et
708 al. 2019), we only considered train-test combinations within similar technologies (one pair of Smart-
709 seq datasets, 10 pairs of 10X datasets). To control for globally encoded differences in expression
710 profiles (correlating with the first principal component), we created random marker sets by picking
711 genes that were expression-matched with meta-analytic markers (decile-matched).

712 Generation of robust meta-marker sets

713 We generated meta-marker sets for each cell type in the MOp hierarchy (Sup. Data 1-3), using the
714 "class", "joint_subclass" and "joint_cluster" annotation levels (see "Meta-analytic hierarchical

715 differential expression statistics"). We kept meta-markers that were either strongly DE (FC>4,
716 FDR<0.05) in at least one dataset or had a meta-analytic FC > 2. We ranked the remaining markers
717 by recurrence, then by AUROC, and selected the top 100 genes (top 50 genes for clusters). If fewer
718 than 100 markers remained, we selected all remaining markers.

719 Cell type annotation of the BICCN isocortex and hippocampus datasets

720 We annotated cells in the isocortex and hippocampus datasets using our robust marker lists (see
721 "Generation of robust marker lists for all BICCN MOp cell types"). To annotate cell types, we adopted
722 a hierarchical cell type annotation procedure. We classified each brain region independently,
723 starting from the log-normalized count matrix. First, we obtained marker scores (average meta-
724 marker expression, see "Marker-based cell type classification") for all cells by running MetaMarker's
725 "score_cells" function. Then, marker scores were converted into cell type predictions using
726 MetaMarker's "assign_cell" function, which finds the marker set with the highest score and returns
727 several QC metric, including the highest score and the marker enrichment (observed score divided
728 by expected score, under the assumption that all marker sets have equal expression). The
729 "assign_cell" function takes two parameters: marker scores and group-level assignments. For
730 subclasses, we provided class-level predictions as the group assignments; for clusters, we provided
731 subclass-level predictions as the group assignments. To filter out cells with unclear assignments, we
732 labeled cells that had a marker enrichment below 1.5 (unless otherwise indicated in the text) as
733 "unassigned".

734 Data and code availability

735 The datasets analyzed during the current study are available in the NeMO archive
736 (https://nemoarchive.org/) at https://assets.nemoarchive.org/dat-ch1nqb7. The full meta-marker
737 lists for the BICCN cell types and optimal number of markers are available on FigShare at

https://doi.org/10.6084/m9.figshare.13348064. The code for MetaMarkers is freely available as an R package on Github at https://github.com/gillislab/MetaMarkers.

Acknowledgments

JG was supported by NIH grants R01MH113005 and R01LM012736. SF was supported by NIH grant U19MH114821.

Declaration of interests

The authors declare that they have no competing financial interests.

Author contributions

SF and JG designed the experiments, performed the data analysis and wrote the paper. All authors read and approved the final manuscript.

Supplemental Material

Supplemental Figure 1. a-c Type S error as a function of AUROC in train datasets (a), marker rank by fold change (b) and marker rank by AUROC (c). The dashed line indicates a type S error of 5%, ribbons around lines indicate variability across cell types and test datasets. **d-g** Type S error as a function of AUROC (d) or FC (e-g) in train dataset, with facets showing variability across hierarchy level (d,e), average cell type size (f) and average gene expression (g). **h** Pareto fronts in FC/AUROC space for inhibitory subclasses. Arrows point to the main historical marker for each subclass. **i** Expression of genes on the Sncg Pareto front across BICCN inhibitory clusters. **j** Pareto fronts in FC/AUROC space for excitatory subclasses. **k** Expression of genes on the L5 ET Pareto front across BICCN excitatory clusters.

758 **Supplemental Figure 2. a-d** Number of perfect markers (a), specific markers (b), sensitive markers
759 (c), and weak markers (d) for BICCN clusters, with cell types ordered according to number of
760 markers, colored according to the dataset used to compute markers. **e-f** MetaNeighbor replicability
761 as a function of the number of specific markers in the scCv2 dataset (e) and the number of perfect
762 markers in the snCv3M dataset (f).

763 **Supplemental Figure 3. a-c** Parametric curve in FC/AUROC space showing evolution of classification
764 performance with an increasing number of marker genes at the class (a), subclass (b) and joint
765 cluster (c) level. **d-g** Breakdown of optimal AUROC performance (meta-analytic markers) as a
766 function of dataset depth, colored by hierarchy level (d), for individual classes, showing variability
767 across test datasets (e), for individual subclasses, showing variability across test datasets (f), for
768 individual clusters, showing variability across test datasets (g). **h-k** Same as d-g with signal-to-noise
769 ratio (FC) at optimal performance instead of AUROC. **l-o** Same as d-g with number of genes at
770 optimal performance instead of AUROC.

771 **Supplemental Figure 4. a-b** Summary of optimal classification performance (F1) across hierarchy
772 levels with transcriptome-wide normalization (a) and marker-wide renormalization (b). Variability is
773 shown across cell types and test datasets. **c-e** Heatmap detailing classification performance for each
774 cell type as a function of the number of genes at the class (c), subclass (d) and cluster (e) level.

775 **Supplemental Figure 5. Top 200 meta-markers show strong, but less specific, enrichment for**
776 **synaptic processes. a** Total number of significantly enriched GO terms (orange) and fraction of
777 significant GO terms that are enriched in a unique cell type (blue) for BICCN classes when an
778 increasing number of meta-markers are considered. **b** Top 3 enriched Gene Ontology (GO) terms for
779 the top 200 meta-markers for each BICCN class. For each dot, the size reflects the False Discovery
780 Rate (FDR), the color reflects the Odds Ratio (OR) of the enrichment test (hypergeometric test). **c**
781 Same as **b** for the top 200 meta-markers for BICCN GABAergic subclasses. **d** Same as **b** for the top
782 200 meta-markers for BICCN Glutamatergic subclasses (only top 2 terms are shown).

783 **Supplemental Figure 6. Meta-analytic markers improve deconvolution performance at every level**
784 **of the hierarchy. a** Schematic of deconvolution task. **b** Summary of deconvolution performance
785 (Pearson's r) at each hierarchy level with 100 markers per cell type. Colors show 3 marker
786 prioritization strategies (single dataset markers, meta-analytic markers or expression-level matched
787 random genes). **c-e** Deconvolution performance (Pearson correlation of true and estimated cell type
788 proportions) for 3 marker prioritization strategies at the class level (c), the subclass level (d), and the
789 cluster level (e). Colors as b.

790 **Supplemental Figure 7. Focus on subclass-level predictions in the auditory cortex. a** Subclass-level
791 predictions in the auditory cortex based on the top 100 meta-markers. Cells remain unassigned (NA)
792 if the enrichment score is lower than 2 for all subclasses. **b** Subclass-level predictions for non-
793 neurons in the auditory cortex based on the top 100 meta-markers (left) and reference labels (right).
794 **c** Subclass-level predictions for Intra-Telencephalic (IT) excitatory neurons in the auditory cortex
795 based on the top 100 meta-markers (left) and reference labels (right).

796 **Supplemental Figure 8. Cluster-level predictions in the auditory cortex. a-c** Cluster-level predictions
797 for Lamp5 inhibitory neurons (a), Near-Projecting (NP) excitatory neurons (b) and layer 2/3 Intra-
798 Telencephalic (IT) excitatory neurons (c) in the auditory cortex based on the top 100 meta-markers
799 (left) and reference labels (right). In all panels, cells remain unassigned (NA) if the enrichment score
800 is lower than 1.5 for all clusters.

801 **Supplemental Figure 9. The marker enrichment score provides robust separability of cell types in**
802 **other cortical regions. a** Marker enrichment scores based on the top 100 meta-markers for the
803 3 BICCN classes in the auditory cortex. The facets are organized according to reference cell types
804 (from the auditory cortex), the x-axis according to meta-markers sets (for the motor cortex). **b** Same
805 as **a** for BICCN inhbitory subclasses. **c** Same as **a** for BICCN excitatory subclasses. **d** Confusion matrix
806 showing the concordance of subclass-level predictions based on the top 100 meta-markers with

807 reference cell types across 40 brain areas. Cells are unassigned if the marker enrichment is lower
808 than 2 for all subclasses.

809 **Supplemental Data 1. Class-level markers.** Top 100 robust markers for BICCN cell types at the class
810 level in CSV format (.csv).

811 **Supplemental Data 2. Subclass-level markers.** Top 100 robust markers for BICCN cell types at the
812 subclass level in CSV format (.csv).

813 **Supplemental Data 3. Cluster-level markers.** Top 50 robust markers for BICCN cell types at the
814 cluster level in CSV format (.csv).

815 References

816 Abbas AR, Wolslegel K, Seshasayee D, Modrusan Z, Clark HF. 2009. Deconvolution of Blood
817 Microarray Data Identifies Cellular Activation Patterns in Systemic Lupus Erythematosus.
818 *PLOS ONE* **4**: e6098.
819 Andrews TS, Hemberg M. 2019. M3Drop: dropout-based feature selection for scRNASeq.
820 *Bioinformatics* **35**: 2865–2867.
821 Ascoli GA, Alonso-Nanclares L, Anderson SA, Barrionuevo G, Benavides-Piccione R, Burkhalter A,
822 Buzsáki G, Cauli B, DeFelipe J, Fairén A, et al. 2008. Petilla terminology: nomenclature of
823 features of GABAergic interneurons of the cerebral cortex. *Nat Rev Neurosci* **9**: 557–568.
824 Asp M, Giacomello S, Larsson L, Wu C, Fürth D, Qian X, Wärdell E, Custodio J, Reimegård J, Salmén F,
825 et al. 2019. A Spatiotemporal Organ-Wide Gene Expression and Cell Atlas of the Developing
826 Human Heart. *Cell* **179**: 1647-1660.e19.
827 Bakken TE, Jorstad NL, Hu Q, Lake BB, Tian W, Kalmbach BE, Crow M, Hodge RD, Krienen FM,
828 Sorensen SA, et al. 2020. Evolution of cellular diversity in primary motor cortex of human,
829 marmoset monkey, and mouse. *bioRxiv* 2020.03.31.016972.
830 Bhaduri A, Andrews MG, Mancia Leon W, Jung D, Shin D, Allen D, Jung D, Schmunk G, Haeussler M,
831 Salma J, et al. 2020. Cell stress in cortical organoids impairs molecular subtype specification.
832 *Nature*.
833 Butler A, Hoffman P, Smibert P, Papalexi E, Satija R. 2018. Integrating single-cell transcriptomic data
834 across different conditions, technologies, and species. *Nat Biotechnol*.
835 http://www.nature.com/doifinder/10.1038/nbt.4096 (Accessed May 7, 2018).
836 Cao J, O'Day DR, Pliner HA, Kingsley PD, Deng M, Daza RM, Zager MA, Aldinger KA, Blecher-Gonen R,
837 Zhang F, et al. 2020. A human cell atlas of fetal gene expression. *Science* **370**.
838 https://science.sciencemag.org/content/370/6518/eaba7721 (Accessed December 1, 2020).
839 Chen M, Zhou X. 2018. VIPER: variability-preserving imputation for accurate gene expression
840 recovery in single-cell RNA sequencing studies. *Genome Biol* **19**: 196.
841 Cobos FA, Alquicira-Hernandez J, Powell J, Mestdagh P, Preter KD. 2020. Comprehensive
842 benchmarking of computational deconvolution of transcriptomics data. *bioRxiv*
843 2020.01.10.897116.
844 Consortium S-I, Su Z, Łabaj PP, Li S, Thierry-Mieg J, Thierry-Mieg D, Shi W, Wang C, Schroth GP,

845 Setterquist RA, et al. 2014. A comprehensive assessment of RNA-seq accuracy,
846 reproducibility and information content by the Sequencing Quality Control Consortium. *Nat*
847 *Biotechnol* **32**: 903–914.
848 Crow M, Gillis J. 2018. Co-expression in Single-Cell Analysis: Saving Grace or Original Sin? *Trends*
849 *Genet* **34**: 823–831.
850 Cui X, Churchill GA. 2003. Statistical tests for differential expression in cDNA microarray experiments.
851 *Genome Biol* **4**: 210.
852 Dong M, Thennavan A, Urrutia E, Li Y, Perou CM, Zou F, Jiang Y. SCDC: bulk gene expression
853 deconvolution by multiple single-cell RNA sequencing references. *Brief Bioinform*.
854 https://academic.oup.com/bib/advance-article/doi/10.1093/bib/bbz166/5699815 (Accessed
855 August 31, 2020).
856 Dumitrascu B, Villar S, Mixon DG, Engelhardt BE. 2019. Optimal gene selection for cell type
857 discrimination in single cell analyses. *bioRxiv* 599654.
858 Gelman A, Carlin J. 2014. Beyond Power Calculations: Assessing Type S (Sign) and Type M
859 (Magnitude) Errors. *Perspect Psychol Sci* **9**: 641–651.
860 Goedhart J, Luijsterburg MS. 2020. VolcaNoseR – a web app for creating, exploring, labeling and
861 sharing volcano plots. *bioRxiv* 2020.05.07.082263.
862 Haghverdi L, Lun ATL, Morgan MD, Marioni JC. 2018. Batch effects in single-cell RNA-sequencing
863 data are corrected by matching mutual nearest neighbors. *Nat Biotechnol* **36**: 421–427.
864 Hicks SC, Townes FW, Teng M, Irizarry RA. 2018. Missing data and technical variability in single-cell
865 RNA-sequencing experiments. *Biostatistics* **19**: 562–578.
866 Hobert O. 2008. Regulatory logic of neuronal diversity: Terminal selector genes and selector motifs.
867 *Proc Natl Acad Sci* **105**: 20067–20071.
868 Hodge RD, Bakken TE, Miller JA, Smith KA, Barkan ER, Graybuck LT, Close JL, Long B, Johansen N,
869 Penn O, et al. 2019. Conserved cell types with divergent features in human versus mouse
870 cortex. *Nature* **573**: 61–68.
871 Huang Q, Liu Y, Du Y, Garmire LX. 2020. Evaluation of Cell Type Annotation R Packages on Single Cell
872 RNA-seq Data. *bioRxiv* 827139.
873 Huang ZJ. 2014. Toward a Genetic Dissection of Cortical Circuits in the Mouse. *Neuron* **83**: 1284–
874 1302.
875 Hunt GJ, Gagnon-Bartsch JA. 2019. The Role of Scale in the Estimation of Cell-type Proportions.
876 *bioRxiv* 857805.
877 Johnson MB, Walsh CA. 2017. Cerebral cortical neuron diversity and development at single-cell
878 resolution. *Curr Opin Neurobiol* **42**: 9–16.
879 Kessaris N, Magno L, Rubin AN, Oliveira MG. 2014. Genetic programs controlling cortical interneuron
880 fate. *Curr Opin Neurobiol* **26**: 79–87.
881 Kharchenko PV, Silberstein L, Scadden DT. 2014. Bayesian approach to single-cell differential
882 expression analysis. *Nat Methods* **11**: 740–742.
883 Kiselev VY, Yiu A, Hemberg M. 2018. scmap: projection of single-cell RNA-seq data across data sets.
884 *Nat Methods* **15**: 359–362.
885 Korsunsky I, Millard N, Fan J, Slowikowski K, Zhang F, Wei K, Baglaenko Y, Brenner M, Loh P,
886 Raychaudhuri S. 2019. Fast, sensitive and accurate integration of single-cell data with
887 Harmony. *Nat Methods* **16**: 1289–1296.
888 Krienen FM, Goldman M, Zhang Q, Rosario R del, Florio M, Machold R, Saunders A, Levandowski K,
889 Zaniewski H, Schuman B, et al. 2019. Innovations in Primate Interneuron Repertoire. *bioRxiv*
890 709501.
891 Lin Y, Ghazanfar S, Wang KYX, Gagnon-Bartsch JA, Lo KK, Su X, Han Z-G, Ormerod JT, Speed TP, Yang
892 P, et al. 2019. scMerge leverages factor analysis, stable expression, and pseudoreplication to
893 merge multiple single-cell RNA-seq datasets. *Proc Natl Acad Sci* **116**: 9775–9784.
894 Liu J, Gao C, Sodicoff J, Kozareva V, Macosko EZ, Welch JD. 2020. Jointly Defining Cell Types from
895 Multiple Single-Cell Datasets Using LIGER. *bioRxiv* 2020.04.07.029546.

896 Lodato S, Arlotta P. 2015. Generating Neuronal Diversity in the Mammalian Cerebral Cortex. *Annu*
897 *Rev Cell Dev Biol* **31**: 699–720.
898 Mancarci BO, Toker L, Tripathy SJ, Li B, Rocco B, Sibille E, Pavlidis P. 2017. Cross-Laboratory Analysis
899 of Brain Cell Type Transcriptomes with Applications to Interpretation of Bulk Tissue Data.
900 *eneuro* **4**: ENEURO.0212-17.2017.
901 Mayer C, Hafemeister C, Bandler RC, Machold R, Batista Brito R, Jaglin X, Allaway K, Butler A, Fishell
902 G, Satija R. 2018. Developmental diversification of cortical inhibitory interneurons. *Nature*
903 **555**: 457–462.
904 Moffitt JR, Bambah-Mukku D, Eichhorn SW, Vaughn E, Shekhar K, Perez JD, Rubinstein ND, Hao J,
905 Regev A, Dulac C, et al. 2018. Molecular, spatial and functional single-cell profiling of the
906 hypothalamic preoptic region. *Science* **362**: eaau5324.
907 Newman AM, Steen CB, Liu CL, Gentles AJ, Chaudhuri AA, Scherer F, Khodadoust MS, Esfahani MS,
908 Luca BA, Steiner D, et al. 2019. Determining cell type abundance and expression from bulk
909 tissues with digital cytometry. *Nat Biotechnol 2019* 1.
910 Packer JS, Zhu Q, Huynh C, Sivaramakrishnan P, Preston E, Dueck H, Stefanik D, Tan K, Trapnell C, Kim
911 J, et al. 2019. A lineage-resolved molecular atlas of C. elegans embryogenesis at single-cell
912 resolution. *Science* **365**. https://science.sciencemag.org/content/365/6459/eaax1971
913 (Accessed December 8, 2020).
914 Patrick E, Taga M, Ergun A, Ng B, Casazza W, Cimpean M, Yung C, Schneider JA, Bennett DA, Gaiteri
915 C, et al. 2020. Deconvolving the contributions of cell-type heterogeneity on cortical gene
916 expression. *PLOS Comput Biol* **16**: e1008120.
917 Paul A, Crow M, Raudales R, He M, Gillis J, Huang ZJ. 2017. Transcriptional Architecture of Synaptic
918 Communication Delineates GABAergic Neuron Identity. *Cell* **171**: 522-539.e20.
919 Pliner HA, Shendure J, Trapnell C. 2019. Supervised classification enables rapid annotation of cell
920 atlases. *Nat Methods* **16**: 983–986.
921 Poulin J-F, Tasic B, Hjerling-Leffler J, Trimarchi JM, Awatramani R. 2016. Disentangling neural cell
922 diversity using single-cell transcriptomics. *Nat Neurosci* **19**: 1131–1141.
923 Qian X, Harris KD, Hauling T, Nicoloutsopoulos D, Muñoz-Manchado AB, Skene N, Hjerling-Leffler J,
924 Nilsson M. 2020. Probabilistic cell typing enables fine mapping of closely related cell types in
925 situ. *Nat Methods* **17**: 101–106.
926 RAMON Y CAJAL S. 1904. Textura del Sistema Nervioso del Hombre y de los Vertebrados, tomo II,
927 primera parte. *Imprenta Libr Nicolas Moya Madr Repr Graf Vidal Leuka Alicante 1992* 399–
928 402.
929 Risso D, Perraudeau F, Gribkova S, Dudoit S, Vert J-P. 2018. A general and flexible method for signal
930 extraction from single-cell RNA-seq data. *Nat Commun* **9**: 284.
931 Schaum N, Karkanias J, Neff NF, May AP, Quake SR, Wyss-Coray T, Darmanis S, Batson J, Botvinnik O,
932 Chen MB, et al. 2018. Single-cell transcriptomics of 20 mouse organs creates a Tabula Muris.
933 *Nature* **562**: 367–372.
934 Shi L, Shi L, Reid LH, Jones WD, Shippy R, Warrington JA, Baker SC, Collins PJ, de Longueville F,
935 Kawasaki ES, et al. 2006. The MicroArray Quality Control (MAQC) project shows inter- and
936 intraplatform reproducibility of gene expression measurements. *Nat Biotechnol* **24**: 1151–
937 1161.
938 Stuart T, Butler A, Hoffman P, Hafemeister C, Papalexi E, Mauck WM, Hao Y, Stoeckius M, Smibert P,
939 Satija R. 2019. Comprehensive Integration of Single-Cell Data. *Cell* **177**: 1888-1902.e21.
940 Svensson V, Vento-Tormo R, Teichmann SA. 2018. Exponential scaling of single-cell RNA-seq in the
941 past decade. *Nat Protoc* **13**: 599–604.
942 Tasic B, Yao Z, Graybuck LT, Smith KA, Nguyen TN, Bertagnolli D, Goldy J, Garren E, Economo MN,
943 Viswanathan S, et al. 2018. Shared and distinct transcriptomic cell types across neocortical
944 areas. *Nature* **563**: 72–78.
945 Tosches MA, Yamawaki TM, Naumann RK, Jacobi AA, Tushev G, Laurent G. 2018. Evolution of
946 pallium, hippocampus, and cortical cell types revealed by single-cell transcriptomics in

947 reptiles. *Science* **360**: 881–888.
948 Tsoucas D, Dong R, Chen H, Zhu Q, Guo G, Yuan G-C. 2019. Accurate estimation of cell-type
949 composition from gene expression data. *Nat Commun* **10**: 2975.
950 Tung PY, Blischak JD, Hsiao CJ, Knowles DA, Burnett JE, Pritchard JK, Gilad Y. 2017. Batch effects and
951 the effective design of single-cell gene expression studies. *Sci Rep* **7**: 39921.
952 Velasco S, Kedaigle AJ, Simmons SK, Nash A, Rocha M, Quadrato G, Paulsen B, Nguyen L, Adiconis X,
953 Regev A, et al. 2019. Individual brain organoids reproducibly form cell diversity of the human
954 cerebral cortex. *Nature* 1.
955 Wang X, Park J, Susztak K, Zhang NR, Li M. 2019. Bulk tissue cell type deconvolution with multi-
956 subject single-cell expression reference. *Nat Commun* **10**: 1–9.
957 Welch JD, Kozareva V, Ferreira A, Vanderburg C, Martin C, Macosko EZ. 2019. Single-Cell Multi-omic
958 Integration Compares and Contrasts Features of Brain Cell Identity. *Cell* **177**: 1873-1887.e17.
959 Yao Z, Liu H, Xie F, Fischer S, Booeshaghi AS, Adkins RS, Aldridge AI, Ament SA, Pinto-Duarte A,
960 Bartlett A, et al. 2020a. An integrated transcriptomic and epigenomic atlas of mouse primary
961 motor cortex cell types. *bioRxiv* 2020.02.29.970558.
962 Yao Z, Nguyen TN, Velthoven CTJ van, Goldy J, Sedeno-Cortes AE, Baftizadeh F, Bertagnolli D, Casper
963 T, Crichton K, Ding S-L, et al. 2020b. A taxonomy of transcriptomic cell types across the
964 isocortex and hippocampal formation. *bioRxiv* 2020.03.30.015214.
965 Yuste R, Hawrylycz M, Aalling N, Aguilar-Valles A, Arendt D, Arnedillo RA, Ascoli GA, Bielza C,
966 Bokharaie V, Bergmann TB, et al. 2020. A community-based transcriptomics classification
967 and nomenclature of neocortical cell types. *Nat Neurosci* 1–13.
968 Zeisel A, Hochgerner H, Lönnerberg P, Johnsson A, Memic F, van der Zwan J, Häring M, Braun E,
969 Borm LE, La Manno G, et al. 2018. Molecular Architecture of the Mouse Nervous System. *Cell*
970 **174**: 999-1014.e22.
971 Zhang M, Eichhorn SW, Zingg B, Yao Z, Zeng H, Dong H, Zhuang X. 2020. Molecular, spatial and
972 projection diversity of neurons in primary motor cortex revealed by in situ single-cell
973 transcriptomics. *bioRxiv* 2020.06.04.105700.
974 Zhang Z, Luo D, Zhong X, Choi JH, Ma Y, Wang S, Mahrt E, Guo W, Stawiski EW, Modrusan Z, et al.
975 2019. SCINA: A Semi-Supervised Subtyping Algorithm of Single Cells and Bulk Samples. *Genes*
976 **10**: 531.
977